



**HAL**  
open science

# Ductile damage modelling with locking-free regularised GTN model

Yi Zhang, Eric Lorentz, Jacques Besson

► **To cite this version:**

Yi Zhang, Eric Lorentz, Jacques Besson. Ductile damage modelling with locking-free regularised GTN model. *International Journal for Numerical Methods in Engineering*, 2018, 113 (13), pp.1871-1903. 10.1002/nme.5722 . hal-03972195

**HAL Id: hal-03972195**

**<https://hal.science/hal-03972195>**

Submitted on 6 Feb 2023




**HAL** is a multi-disciplinary open access archive for the deposit and dissemination of scientific research documents, whether they are published or not. The documents may come from teaching and research institutions in France or abroad, or from public or private research centers.

L'archive ouverte pluridisciplinaire **HAL**, est destinée au dépôt et à la diffusion de documents scientifiques de niveau recherche, publiés ou non, émanant des établissements d'enseignement et de recherche français ou étrangers, des laboratoires publics ou privés.



Distributed under a Creative Commons Attribution - NonCommercial 4.0 International License

# Ductile damage modelling with locking-free regularised GTN model

Yi Zhang<sup>1,2</sup>  | Eric Lorentz<sup>1</sup>  | Jacques Besson<sup>2</sup> 

<sup>1</sup>EDF R&D, Department of Electrotechnique et Mécanique des Structures, 7 Boulevard Gaspard Monge, Palaiseau 91120, France

<sup>2</sup>Mines ParisTech, PSL Research University, Centre des Matériaux, UMR CNRS 7633, 10 rue Henri Desbruères, Evry 91000, France

## Correspondence

Yi Zhang, Mines ParisTech, PSL Research University, Centre des Matériaux, UMR CNRS 7633, 10 rue Henri Desbruères, Evry 91000, France.  
Email: yi.zhang@mines-paristech.fr

## Summary

The major goal of this work is to develop a robust modelling strategy for the simulation of ductile damage development including crack initiation and subsequent propagation. For that purpose, a Gurson-type model is used. This model class, as many other damage models, leads to significant material softening and must be used within a large deformation framework due to the ductile character of the materials. This leads to 2 main difficulties that should be dealt with carefully: mesh dependency and volumetric locking. In this work, a logarithmic finite strain framework is adopted in which the Gurson-Tvergaard-Needleman constitutive law is reformulated. Then a nonlocal formulation with regularisation of hardening variable is applied so as to solve mesh dependency and strain localization problem. In addition, the nonlocal model is combined with mixed “displacement-pressure-volume variation” elements to avoid volumetric locking. Thereby, a mesh-independent and locking-free finite strain framework suitable for the modelling of ductile rupture is established. Attention is paid to mathematical properties and numerical performance of the model. Finally, the model parameters are identified on an experimental database for a nuclear piping steel. Simulations of standard test specimens (notched tensile bars and compact tension and single edge notched tensile cracked specimens) are performed and compared to experimental results.

## KEYWORDS

ductile damage, GTN model, mesh dependency, mixed finite element, nonlocal regularisation, volumetric locking

## 1 | INTRODUCTION

Ductile fracture is characterised by large plastic deformation so that plastic energy dissipation cannot be neglected as in brittle fracture. Material deterioration accompanied by this high level of energy dissipation before fracture is considered as ductile damage. In the last decades, numerical models based on micromechanical analyses have been found appealing to represent ductile damage. In accordance with experimental observations, models are usually based on the description of the evolution of cavities/voids leading to the initiation of a macroscopic crack. It involves 3 distinct steps: (i) cavity nucleation, (ii) cavity growth, and (iii) cavity coalescence.<sup>1</sup> Among ductile damage models, micromechanical models based on the seminal work of Gurson<sup>2</sup> are the most widely used. The model introduces the void volume fraction as a damage variable, which is used to describe the effect of damage on the material yield surface. The resulting yield surface is pressure sensitive. This dependence together with the use of the normality rule allows deriving the evolution of the void volume

fraction in absence of void nucleation. The initial Gurson model was derived from rigorous mechanical analysis of the growth of a spherical void in a rigid perfectly plastic material. The model was then extended phenomenologically by Tvergaard and Needleman<sup>3</sup> in order to (i) introduce elastic strain, (ii) introduce work hardening, (iii) cover the cavity evolution up to coalescence, and (4) get a better agreement with experiments. In recent years, studies based on Gurson-type models have led to numerous extensions principally aiming at a better physical description of ductile damage (see review in Besson<sup>4</sup> and Benzerga and Leblond<sup>5</sup>). The use of these extensions allows simulating laboratory size specimens for which a good agreement is found with experiments on several specimens such as notched axisymmetric tensile bar and cracked tensile specimen (see, eg, Springman and Kuna<sup>6</sup> and Enakoutsa and Leblond<sup>7</sup>). Despite the fact that the most recent extensions of the Gurson model greatly improve the description of the physics of damage, these models are still clearly facing several severe numerical difficulties when used in finite element (FE) softwares, which should be dealt carefully.

Fracture simulations based on local continuum damage models are generally faced with mesh dependency: The numerical results may strongly depend on the FE discretization: element type, element size, element orientation, etc. This well-known numerical problem results from the ill-posedness in the damage governing differential equation,<sup>8</sup> and regularisation techniques are often proposed to solve the problem. Several regularisation techniques based on non-local models are found in the literature. The 2 most popular methods are the convolution method<sup>9</sup> and gradient method.<sup>10,11</sup> The principle of these approaches is to introduce a spatial coupling term in the constitutive equation so as to redistribute the strain and damage fields and to avoid pathological localization. Different variables can be chosen as regularised variable; this includes the plastic strain tensor,<sup>7</sup> the volume variation,<sup>12</sup> the hydrostatic plastic strain,<sup>13</sup> the equivalent plastic strain,<sup>12,14</sup> and the damage variable.<sup>15</sup>

Another problem observed in ductile damage simulation is the volumetric locking, which results from plastic quasi-incompressibility. Volumetric locking leads to strong oscillations of the pressure field and alters the convergence of the computation. Since traditional (ie, displacement based) FEs are not capable of accurately calculating stress fields for a quasi-incompressible behaviour at Gauss point level, some enhanced elements have been developed over the last years and perform well in quasi-incompressible situations. The work of Al-Akhrass et al<sup>16</sup> based on Taylor<sup>17</sup> proposes a mixed element where volume variation and pressure are introduced as 2 additional nodal variables in addition to the displacements.

In the present paper, a nonlocal Gurson-Tvergaard-Needleman (GTN) model based on a logarithmic finite strain formulation<sup>18</sup> is chosen to model ductile damage. To avoid mesh dependency, a regularisation method using the gradient of equivalent plastic strain is introduced. Besides, the mixed element formulation is coupled with the nonlocal model to solve the volumetric locking. The paper proceeds as follows: In Section 2, the theoretical part of the proposed model including the logarithmic finite strain formulation, the nonlocal version of GTN model, and the mixed element are presented. In Section 3, the FE algorithm to solve the governing equations is explained, and its robustness is also demonstrated. Finally, the proposed simulation strategy is applied to represent an existing experimental database for a nuclear piping steel in Section 4.

## 2 | KINEMATIC FORMULATION AND GTN CONSTITUTION EQUATIONS

### 2.1 | A logarithmic finite strain formulation for standard J2 plasticity

A finite strain formulation is required for ductile damage modelling because of the large deformation. Here, a logarithmic formulation based on the work of Miehe et al<sup>18</sup> is applied. The main steps are recalled in the following. The logarithmic strain tensor is defined as

$$\mathbf{E} = \frac{1}{2} \ln(\mathbf{F}^T \cdot \mathbf{F}) = \frac{1}{2} \ln(\mathbf{C}). \quad (1)$$

The stress tensor  $\mathbf{T}$  is defined by duality with respect to the logarithmic strain rate:

$$\mathcal{P}_i = \int_{\Omega_0} \boldsymbol{\tau} : \mathbf{D} \, d\Omega_0 = \int_{\Omega_0} \mathbf{T} : \dot{\mathbf{E}} \, d\Omega_0. \quad (2)$$

This gives the relation between the Kirchhoff stress tensor  $\boldsymbol{\tau}$  and  $\mathbf{T}$ . Indeed, differentiating (1) leads to

$$\delta \mathbf{E} = \frac{\partial \mathbf{E}}{\partial \mathbf{C}} : \delta \mathbf{C} = \mathbb{P} : (\mathbf{F}^T \cdot \delta \mathbf{F}) \quad \text{with} \quad \mathbb{P} = \frac{2 \partial \mathbf{E}}{\partial \mathbf{C}}(\mathbf{C}). \quad (3)$$

Then, equating both sides of (2) for any  $\dot{\mathbf{F}}$  results in

$$\boldsymbol{\tau} = \mathbf{F}(\mathbf{T}:\mathbb{P})\mathbf{F}^T. \quad (4)$$

Note that thanks to the stress definition (2), the variational formulation of the equilibrium equations reads

$$\forall \delta \mathbf{u} \quad \int_{\Omega_0} \mathbf{T}:\mathbb{P}:(\mathbf{F}^T \cdot \nabla \delta \mathbf{u}) \, d\Omega_0 = \delta \mathcal{W}_{ext}, \quad (5)$$

where  $\mathcal{W}_{ext}$  stands for the potential of external forces and  $\delta \mathbf{u}$  is classically subjected to the constraint of kinematical admissibility.

In the context of isotropic plasticity, the material state is described by the current strain, the hardening variable  $\kappa$ , and the plastic strain  $\mathbf{E}^p$ , where the logarithmic strain is additively split into an elastic part and a plastic part:

$$\mathbf{E} = \mathbf{E}^e + \mathbf{E}^p. \quad (6)$$

The Helmholtz free energy density, ie, the energy per unit volume in the reference configuration, is classically split into the elastic strain energy  $\Phi^e$  and the stored energy due to work hardening  $\Phi^p$  without state coupling:

$$\Phi = \Phi(\mathbf{E}, \mathbf{E}^p, \kappa) = \Phi^e(\mathbf{E} - \mathbf{E}^p) + \Phi^p(\kappa). \quad (7)$$

Thanks to the duality introduced in (2), the dissipation rate reads

$$D = \mathbf{T}:\dot{\mathbf{E}} - \dot{\Phi} = \left( \mathbf{T} - \frac{\partial \Phi}{\partial \mathbf{E}} \right) : \dot{\mathbf{E}} - \frac{\partial \Phi}{\partial \mathbf{E}^p} : \dot{\mathbf{E}}^p - \frac{\partial \Phi}{\partial \kappa} \dot{\kappa}. \quad (8)$$

The first term should be equal to zero for any reversible evolution, which provides the definition of the stress:

$$\mathbf{T} = \frac{\partial \Phi}{\partial \mathbf{E}} = \frac{\partial \Phi^e}{\partial \mathbf{E}^e}. \quad (9)$$

Thus, the stress-strain relation is of hyperelastic type and does not require the introduction of an objective stress rate. The dissipation rate reduces to the following expression, with  $A$  being the driving force for the hardening mechanisms:

$$D = \mathbf{T}:\dot{\mathbf{E}}^p + A \dot{\kappa} \quad \text{where} \quad A = - \frac{\partial \Phi}{\partial \kappa} = - \frac{\partial \Phi^p}{\partial \kappa}. \quad (10)$$

Regarding the evolution equations, the generalised standard material framework<sup>19</sup> is used. It corresponds here to the principle of maximal dissipation with respect to a yield surface, which depends on  $\mathbf{T}$  and  $A$  through a threshold function  $F(\mathbf{T}, A)$ . This leads to the following normal flow rules and consistency condition, with  $\lambda$  being the plastic multiplier:

$$\begin{aligned} \dot{\mathbf{E}}^p &= \lambda \frac{\partial F}{\partial \mathbf{T}}, & \dot{\kappa} &= \lambda \frac{\partial F}{\partial A} \\ \lambda F(\mathbf{T}, A) &= 0, & F(\mathbf{T}, A) &\leq 0, & \lambda &\geq 0. \end{aligned} \quad (11)$$

Note that the time derivative in  $\dot{\mathbf{E}}^p$  is objective since the strain  $\mathbf{E}$  (hence, the plastic strain  $\mathbf{E}^p$ ) refers to the reference configuration.

Finally, the elastoplastic constitutive relation is characterised by the elastic strain energy  $\Phi^e$ , the hardening strain energy  $\Phi^p$ , and the threshold function  $F$ . Note that for metallic materials, the elastic part of the strain remains small so that the elastic strain energy may retain its usual quadratic expression:

$$\Phi^e(\mathbf{E}^e) = \frac{1}{2} \mathbf{E}^e : \mathbb{E} : \mathbf{E}^e. \quad (12)$$

In particular, in the case of isotropic materials as considered in this presentation, the Hooke tensor reads, with  $K$  the bulk modulus and  $\mu$  the shear modulus,

$$\mathbb{E}:\mathbf{E}^e = K \text{tr}(\mathbf{E}^e) \mathbf{I} + 2\mu \text{dev}(\mathbf{E}^e). \quad (13)$$

## 2.2 | The local GTN constitutive equations

The purpose of this part is to cast the GTN constitutive law into the previous logarithmic setting for plasticity. Two points will need a specific attention:

- In the GTN model, the porosity (the void volume fraction) shrinks the elasticity domain; this is responsible for the softening character. Therefore, the yield surface depends on the porosity, a characteristic that should be taken into account in the evolution law (11). Moreover, the porosity evolution is governed by an additional equation, which accounts for the plastic incompressibility of the matrix and possible nucleation (as detailed in the following).
- The hardening mechanism in the GTN model does not follow a flow rule in the same way as in (11). Hence, it will require a reformulation.

In the original presentation of the GTN model,<sup>3</sup> the yield surface relies on the porosity  $f$  and on the hardening parameter  $\kappa$  through the following threshold function:

$$F_{\text{GTN}}(\boldsymbol{\sigma}) = \left( \frac{\sigma_{\text{eq}}}{\bar{\sigma}(\kappa)} \right)^2 + 2q_1 f^* \cosh \left( \frac{q_2 \text{tr} \left( \frac{\boldsymbol{\sigma}}{\bar{\sigma}(\kappa)} \right)}{2} \right) - 1 - (q_1 f^*)^2 \leq 0. \quad (14)$$

In the former expression,  $q_1$  and  $q_2$  are material parameters,  $\boldsymbol{\sigma}$  is the Cauchy stress tensor, and  $\bar{\sigma}(\kappa)$  is the current flow stress. Besides,  $f^*$  denotes an effective porosity, which models the coalescence phenomenon in a coarse way by increasing the effect of porosity on the yield surface above a critical coalescence porosity  $f_c$ :

$$f^* = \begin{cases} f & \text{if } f \leq f_c \\ f_c + \delta(f - f_c) & \text{if } f > f_c \end{cases} \quad \text{where } \delta = \frac{1/q_1 - f_c}{f_f - f_c}. \quad (15)$$

Here,  $f_f$  denotes the fracture porosity. When it is reached, only  $\boldsymbol{\sigma} = \mathbf{0}$  is admissible according to (14).

An alternative but strictly equivalent expression of (14) is proposed in Besson et al.<sup>20</sup> It relies on the introduction of a scalar stress measure  $\sigma_* = N(\boldsymbol{\sigma})$ , which is a positive homogeneous function of degree 1 of the stress tensor; it plays the same role as the equivalent stress for the von Mises criterion. This measure  $N$ , which also depends on  $f^*$ , is implicitly defined as follows as long as  $q_1 f^* < 1$ :

$$\left| \begin{array}{l} \text{Find } \sigma_* = N(\boldsymbol{\sigma}) \quad \text{such that } G(\boldsymbol{\sigma}, \sigma_*, f^*) = 0 \\ \text{with } G(\boldsymbol{\sigma}, \sigma_*, f^*) \stackrel{\text{def}}{=} \left( \frac{\sigma_{\text{eq}}}{\sigma_*} \right)^2 + 2q_1 f^* \cosh \left( \frac{q_2 \text{tr} \left( \frac{\boldsymbol{\sigma}}{\sigma_*} \right)}{2} \right) - 1 - (q_1 f^*)^2. \end{array} \right. \quad (16)$$

For the sake of completeness, the extension to the case  $q_1 f^* = 1$  corresponds to

$$N(\boldsymbol{\sigma}) = \begin{cases} 0 & \text{if } \boldsymbol{\sigma} = \mathbf{0} \\ +\infty & \text{if } \boldsymbol{\sigma} \neq \mathbf{0} \end{cases}. \quad (17)$$

As the function  $G$  is convex with respect to  $\boldsymbol{\sigma}$ , it can be shown that  $N$  is also a convex function. Thanks to this definition, the elasticity domain is then simply characterised by

$$\sigma_* - \bar{\sigma}(\kappa) \leq 0. \quad (18)$$

The next step consists in expressing the yield surface as a function of the dual stress  $\mathbf{T}$  rather than the Cauchy stress  $\boldsymbol{\sigma}$ . Replacing rigorously  $\boldsymbol{\sigma}$  by its expression as a function of  $\mathbf{T}$  and  $\mathbf{F}$  is a straightforward approach, but it would lead to a poorly practical threshold function. One however notices that (i) the dual stress  $\mathbf{T}$  and the Kirchhoff stress  $\boldsymbol{\tau} = J\boldsymbol{\sigma}$  always admit the same trace and (ii) if the local evolution is such that  $\dot{\mathbf{E}}$  remains coaxial to  $\mathbf{E}$ , then  $\mathbf{T}$  and  $\boldsymbol{\tau}$  admit the same invariants (hence,  $T_{\text{eq}} = \tau_{\text{eq}}$ ). Therefore, (18) can be expressed as a function of  $\boldsymbol{\tau}$ , leading to an expression strictly equivalent to (18):

$$\frac{N(\boldsymbol{\tau})}{J} - \bar{\sigma}(\kappa) \leq 0. \quad (19)$$

This expression is then approximated by using  $\mathbf{T}$  instead of  $\boldsymbol{\tau}$ , which results in a yield surface close to the original GTN one:

$$\frac{N(\mathbf{T})}{J} - \bar{\sigma}(\kappa) \leq 0. \quad (20)$$

In that way, only the Jacobian of the deformation  $J$  is involved in the expression of the yield surface and not all the components of  $\mathbf{F}$  in a cumbersome way. In agreement with the logarithmic strain setting, the normality with respect to the yield surface then provides the plastic strain rate direction and the consistency condition:

$$\dot{\mathbf{E}}^p = \frac{\lambda \partial N}{J \partial \mathbf{T}}, \quad (21)$$

$$\lambda \geq 0 \quad ; \quad \frac{N(\mathbf{T})}{J} - \bar{\sigma}(\kappa) \leq 0 \quad ; \quad \lambda \left[ \frac{N(\mathbf{T})}{J} - \bar{\sigma}(\kappa) \right] = 0. \quad (22)$$

Concerning the evolution of the hardening variable, the original GTN law provides the following evolution equation:

$$\boldsymbol{\sigma} : \mathbf{D}^p = (1-f) \bar{\sigma}(\kappa) \dot{\kappa}. \quad (23)$$

Following the definition of  $\mathbf{T}$  in (2), this can be rewritten as:

$$\frac{1}{J} \mathbf{T} : \dot{\mathbf{E}}^p = (1-f) \bar{\sigma}(\kappa) \dot{\kappa} \quad (24)$$

Thanks to the flow rule (21), the consistency condition (22) and the fact that  $N$  is positive homogeneous of degree 1, one has by means of the Euler identity:

$$\mathbf{T} : \dot{\mathbf{E}}^p = \frac{\lambda}{J} \mathbf{T} : \frac{\partial N}{\partial \mathbf{T}} = \frac{\lambda}{J} N(\mathbf{T}) = \lambda \bar{\sigma}(\kappa). \quad (25)$$

From (24) and (25), one deduces the evolution law for the hardening variable:

$$\dot{\kappa} = \lambda \frac{1}{(1-f)J}. \quad (26)$$

When considering the evolution of the porosity, it will be shown that  $(1-f)J \approx 1$ , provided that the nucleation part of the porosity and the initial porosity are small. In that case, (26) reduces to

$$\dot{\kappa} = \lambda. \quad (27)$$

Note that the error resulting from this approximation leads to a small error on the hardening variable and on the flow stress, with minimal impact on the model response (in particular, when the hardening function is identified so as to fit an experimental result). At this stage, the threshold function  $F(\mathbf{T}, A)$  can be derived from (11), (21), and (27) through

$$\left. \begin{aligned} \dot{\mathbf{E}}^p = \lambda \frac{\partial F}{\partial \mathbf{T}} = \frac{\lambda \partial N}{J \partial \mathbf{T}} &\Rightarrow \frac{\partial F}{\partial \mathbf{T}} = \frac{1 \partial N}{J \partial \mathbf{T}} \\ \dot{\kappa} = \lambda \frac{\partial F}{\partial A} = \lambda &\Rightarrow \frac{\partial F}{\partial A} = 1 \end{aligned} \right\} \Rightarrow F(\mathbf{T}, A) = \frac{N(\mathbf{T})}{J} + A - \sigma^0, \quad (28)$$

with  $\sigma^0$  being the initial yield stress. Moreover, comparing the consistency conditions (11) and (22) provides the expression of the hardening driving force  $A$ :

$$A = -(\bar{\sigma}(\kappa) - \sigma^0). \quad (29)$$

Thanks to the choice of  $\sigma^0$  as the integration constant in (28), the hardening driving force is initially equal to zero. Then the stored energy  $\Phi^P$  can be calculated, thanks to the expression of  $A$ :

$$\Phi^P(\kappa) = - \int_0^\kappa A \, d\kappa = \int_0^\kappa (\bar{\sigma}(s) - \sigma^0) \, ds. \quad (30)$$

The yield threshold and the flow rules have been cast into the framework of generalised standard materials for a given porosity. It now remains to explicate the evolution equation for the latter. The original proposal for the GTN model takes into account 2 components, one related to nucleation of cavity, the other resulting from cavity growth:

$$\dot{f} = \dot{f}_n + \dot{f}_g \quad \text{with} \quad \dot{f}_n = B_n(\kappa) \dot{\kappa} \quad \text{and} \quad \dot{f}_g = (1-f) \text{tr} \mathbf{D}^P. \quad (31)$$

The initial condition takes care of the initial porosity  $f_0$  through, for instance,  $f_g(0) = f_0$  and  $f_n(0) = 0$ . Regarding the nucleation part, a usual choice is

$$B_n(\kappa) = \frac{f_N}{s_N \sqrt{2\pi}} \exp \left[ -\frac{1}{2} \left( \frac{\kappa - \kappa_N}{s_N} \right)^2 \right], \quad (32)$$

where 3 additional material parameters  $f_N$ ,  $s_N$ ,  $\kappa_N$  are introduced. The differential equation for  $f_n$  admits an explicit solution by integrating  $\dot{f}_n$  of (31), where erf denotes the error function:

$$f_n(\kappa) = \frac{f_N}{2} \left[ \text{erf} \left( \frac{\kappa_N}{s_N \sqrt{2}} \right) + \text{erf} \left( \frac{\kappa - \kappa_N}{s_N \sqrt{2}} \right) \right]. \quad (33)$$

This integrated expression is advantageous because it avoids numerical errors, which could otherwise occur for small values of  $s_N$ . The evolution of the second part of the porosity, related to the cavity growth, can be reformulated with the plastic strain  $\mathbf{E}^P$ . Indeed, one can notice that

$$\text{tr} \mathbf{D}^P = \frac{d}{dt} (\ln J^P) = \text{tr} \dot{\mathbf{E}}^P, \quad (34)$$

where  $J^P$  is the part of the Jacobian related to plastic volumetric variation. Therefore, the evolution of  $f_g$  simply reads

$$\dot{f}_g = (1-f) \text{tr} \dot{\mathbf{E}}^P. \quad (35)$$

Note that thanks to the plasticity flow rules (28), the porosity evolution is hence related to the evolution of the hardening variable:

$$\dot{f}_g = \dot{\kappa} (1-f) \frac{\partial \mathbf{F}}{\partial \mathbf{T}} : \mathbf{I}. \quad (36)$$

This concludes the equations of the GTN model cast into the logarithmic setting for plasticity. One can notice that the evolution equation for the porosity does not follow a normality flow rule with respect to the yield threshold. Therefore, the whole model does not belong to the framework of generalised standard materials. Nevertheless, one should remind that it does belong to the framework for a fixed porosity, a property that will be used below for its interesting numerical implications.

At last, for the sake of completeness, one can now justify the approximation  $(1-f)J \approx 1$  used in (27). Indeed, the evolution equation (31) can be rewritten as

$$\frac{\dot{f}}{1-f} = \frac{d}{dt} (\ln J^P) + \frac{\dot{f}_n}{1-f}. \quad (37)$$

Integrating with respect to time and introducing the multiplicative split  $J = J^e J^p$  leads to

$$(1-f)J = J^e(1-f_0) \exp \left[ - \int_0^t \frac{\dot{f}_n(\tau)}{1-f(\tau)} d\tau \right]. \quad (38)$$

Finally, a Taylor expansion allows justifying the approximation since

$$(1-f)J = 1 + O(f_0) + O\left(\frac{f_n}{1-f}\right) + O(|J^e-1|). \quad (39)$$

### 2.3 | A nonlocal GTN model with gradient constitutive relations

It can be noticed that the elasticity domain in the Cauchy stress space as defined in (18) decreases with increasing porosity. This shrinkage enters progressively in competition with the hardening mechanism related to the increase of the flow stress  $\bar{\sigma}(\kappa)$  and finally prevails, leading to the softening of the constitutive law after an initial hardening phase. As recalled in the introduction, softening constitutive laws lead to ill-posed boundary value problems so that a nonlocal formulation is required for physical as well as mathematical reasons. Here, it is proposed to introduce the nonlocality through the gradient of the hardening variable. Indeed, this choice is thought to control simultaneously (i) the plastic localization, which may result from geometrical considerations (necking) or numerical ones (spurious artefacts related to the FEs used to relax the volumetric locking due to plastic incompressibility), and (ii) the porosity localization, which results from strain softening since the porosity evolution is related to  $\dot{\kappa}$  through (33) and (36).

More precisely, the gradient of the hardening variable  $\underline{\nabla}\kappa$  is introduced into the Helmholtz free energy density (7).

$$\Phi_{nl}(\mathbf{E}, \mathbf{E}^p, \kappa, \underline{\nabla}\kappa) = \Phi^e(\mathbf{E}-\mathbf{E}^p) + \Phi^p(\kappa) + \frac{c}{2}\underline{\nabla}\kappa \cdot \underline{\nabla}\kappa. \quad (40)$$

The strictly positive parameter  $c$ , which has the dimension of a force, weights the nonlocal interactions between neighbour material points. The latter precludes uncontrolled localisation of the hardening variable since they would result in an infinite free energy: The larger the parameter  $c$ , the smoother the spatial distribution of the hardening variable.

A framework for constitutive laws with gradient of internal variables has been proposed in Lorentz.<sup>21</sup> It suggests that the appropriate scale for handling such constitutive relations is the scale of the structure. Therefore, the global Helmholtz free energy is introduced, as in Nguyen et al<sup>22</sup>:

$$\mathcal{F}(u, \kappa, \mathbf{E}^p) = \int_{\Omega_0} \Phi_{nl}(\mathbf{E}(u), \mathbf{E}^p, \kappa, \underline{\nabla}\kappa) d\Omega_0. \quad (41)$$

The global dissipation retains its usual definition:

$$\mathcal{D} = \int_{\Omega_0} \mathbf{T} : \dot{\mathbf{E}} d\Omega_0 - \dot{\mathcal{F}}. \quad (42)$$

After differentiation and application of the Green formula, it reads

$$\begin{aligned} \mathcal{D} = \int_{\Omega_0} \left[ \left( \mathbf{T} - \frac{\partial \Phi_{nl}}{\partial \mathbf{E}} \right) : \dot{\mathbf{E}} - \frac{\partial \Phi_{nl}}{\partial \mathbf{E}^p} : \dot{\mathbf{E}}^p + \left( - \frac{\partial \Phi_{nl}}{\partial \kappa} + \operatorname{div} \left( \frac{\partial \Phi_{nl}}{\partial \underline{\nabla}\kappa} \right) \right) \dot{\kappa} \right] d\Omega_0 \\ + \int_{\partial\Omega_0} \left( - \frac{\partial \Phi_{nl}}{\partial \underline{\nabla}\kappa} \cdot \underline{n} \right) \dot{\kappa} dS. \end{aligned} \quad (43)$$

Again, for reversible evolution, the dissipation should be zero. This implies that the stress-strain relation retains its former hyperelastic definition, thanks to the fact that no derivative of the strain tensor is introduced into the constitutive law, and according to (9), (12), and (40):



$$\mathbf{T} = \frac{\partial \Phi_{nl}}{\partial \mathbf{E}} = \frac{\partial \Phi^e}{\partial \mathbf{E}^e} = \mathbb{E}:(\mathbf{E}-\mathbf{E}^p). \quad (44)$$

Then, the dissipation can be rewritten as

$$\mathcal{D} = \int_{\Omega_0} \left[ \mathbf{T}:\dot{\mathbf{E}}^p + \left( -\frac{\partial \Phi^p}{\partial \kappa} + \text{div}(c \nabla \kappa) \right) \dot{\kappa} \right] d\Omega_0 + \int_{\partial\Omega_0} \left( -c \nabla \kappa \cdot \underline{n} \right) \dot{\kappa} dS. \quad (45)$$

In particular, one can notice that the driving force associated with the plastic strain tensor is still the stress tensor while the driving force associated with the hardening variable involves now a nonlocal term in addition to its former expression (10):

$$A_{nl} = -\frac{\partial \Phi^p}{\partial \kappa} + \text{div}(c \nabla \kappa) = \sigma_0 - \bar{\sigma}(\kappa) + \text{div}(c \nabla \kappa). \quad (46)$$

It is chosen to preserve the evolution equations as in the local GTN model (11) but with the new expressions of the driving forces:

$$\dot{\mathbf{E}}^p = \frac{\lambda}{J} \frac{\partial \mathbf{N}}{\partial \mathbf{T}} ; \quad \dot{\kappa} = \lambda, \quad (47)$$

$$\lambda \geq 0 ; \quad \frac{\mathbf{N}(\mathbf{T})}{J} - \bar{\sigma}(\kappa) + \text{div}(c \nabla \kappa) \leq 0 ; \quad \lambda \left[ \frac{\mathbf{N}(\mathbf{T})}{J} - \bar{\sigma}(\kappa) + \text{div}(c \nabla \kappa) \right] = 0. \quad (48)$$

One can notice that for a homogeneous parameter  $c$ , a Laplacian term emerges in the yield condition, as introduced in gradient plasticity.<sup>23,24</sup> Besides, the evolution of the porosity is modelled as in the local GTN law presented above.

Moreover, it is assumed that no dissipation stems from the boundary (this is a constitutive assumption corresponding to no surface energy), an assumption already stated for brittle materials, see Sicsic et al.<sup>25</sup> In that case, the boundary term in the dissipation (45) should be equal to zero whatever the admissible evolution of the hardening variable, which results in the following boundary condition (assuming that the initial hardening variable  $\kappa$  is equal to zero everywhere):

$$c \nabla \kappa \cdot \underline{n} = 0 \quad \text{on } \partial\Omega_0. \quad (49)$$

This defines finally the proposed nonlocal GTN model. The constitutive equations are gathered in box 1, where the former local model can be retrieved by setting  $c=0$ . A relaxed version of this model, which is more suitable for FE implementation, is detailed in the next section.

Box 1 – Nonlocal GTN constitutive relation (original and relaxed versions)

Stress-strain relation

$$\mathbf{T} = \mathbb{E}:(\mathbf{E}-\mathbf{E}^p)$$

Implicit definition of the GTN equivalent stress  $T^*$

$$G(\mathbf{T}, T_*, f^*) = \left( \frac{T_{\text{eq}}}{T_*} \right)^2 + 2q_1 f^* \cosh \left( \frac{q_2 \text{tr} \left( \frac{\mathbf{T}}{T_*} \right)}{2} \right) - 1 - (q_1 f^*)^2 = 0$$

Definition of the relaxed yield surface

$$F(\mathbf{T}, A_{nl}) = \frac{T_*}{J} - \bar{\sigma}(\kappa) + \text{div}(c \nabla \kappa) \quad (\text{original version, Section 2.3})$$

$$F(\mathbf{T}, A_{rlx}) = \frac{T_*}{J} - \bar{\sigma}(\kappa) + l + r(a-\kappa) \quad (\text{relaxed version, Section 3.1})$$

Flow rules

$$\dot{\mathbf{E}}^p = \frac{\lambda}{J} \frac{\partial T^*}{\partial \mathbf{T}} ; \quad \dot{\kappa} = \lambda$$

Consistency condition

$$\lambda \geq 0 ; \quad F \leq 0 ; \quad \lambda F = 0$$

Porosity evolution

$$f = f_n(\kappa) + f_g ; \quad \dot{f}_g = (1-f) \operatorname{tr} \dot{\mathbf{E}}^p$$

Coalescence

$$f^* = \begin{cases} f & \text{if } f \leq f_c \\ f_c + \delta(f - f_c) & \text{if } f > f_c \end{cases} \quad \text{where } \delta = \frac{1/q_1 - f_c}{f_f - f_c}$$

### 3 | GOVERNING EQUATIONS AND NUMERICAL IMPLEMENTATION

#### 3.1 | Treatment of nonlocality

In the previous section, a nonlocal formulation has been proposed for the GTN model. In practice, the nonlocality stems from the Laplacian term that has been introduced into the consistency equation (48). On a numerical ground, the consequences are immediate. Indeed, in the case of a local constitutive relation, the treatment of the constitutive law is generally pointwise, which means that it can be done independently from one integration point to another: the output variables (stress and internal variables) are sampled at the integration points. The spatial coupling (the strain-displacement relation and the equilibrium equation) is dealt on a global level, where the displacement is a nodal variable. Such a split is a priori precluded here since the nonlocality involves the constitutive law itself: the nonlinearity resulting from the constitutive law (in particular, because of the plasticity threshold) is mingled with the spatial nonlocality. Fortin and Glowinski<sup>26</sup> proposed a numerical method they named decomposition-coordination to deal with such a coupling in the case of optimisation problems. The idea is based on a relaxation, which consists in duplicating the variable of interest: One instance of the variable is dedicated to nonlocality and the other one to nonlinearity. A Lagrangian multiplier is introduced to enforce the equality between both instances. In addition a penalty term may also be introduced so as to enforce the former relation and to provide additional coercivity.

Consider now the application of this method to the nonlocal GTN model. The starting point is the global Helmholtz free energy where the local and nonlocal parts are highlighted:

$$\begin{aligned} \mathcal{F}(u, \kappa, \mathbf{E}^p) &= \mathcal{F}_{loc}(u, \kappa, \mathbf{E}^p) + \mathcal{F}_{gdt}(\kappa) \\ \mathcal{F}_{loc}(u, \kappa, \mathbf{E}^p) &= \int_{\Omega_0} \Phi^e(\mathbf{E}(u) - \mathbf{E}^p) + \Phi^p(\kappa) \, d\Omega_0 ; \quad \mathcal{F}_{gdt}(\kappa) = \int_{\Omega_0} \frac{c}{2} \nabla \kappa \cdot \nabla \kappa \, d\Omega_0. \end{aligned} \quad (50)$$

The hardening variable  $\kappa$  is duplicated: the local instance is still denoted  $\kappa$  while the nonlocal one is denoted  $a$ . To enforce the equality  $a = \kappa$ , a Lagrangian term and a penalty term are introduced into the energy, where the Lagrange multiplier is denoted  $l$  and the penalty coefficient is  $r > 0$ . The relaxed Helmholtz free energy, which is denoted  $\mathcal{L}$  (it is a Lagrangian), is the following:

$$\begin{aligned} \mathcal{L}(u, a, l, \kappa, \mathbf{E}^p) &= \mathcal{F}_{loc}(\mathbf{E}(u), \mathbf{E}^p, \kappa) + \mathcal{F}_{gdt}(a) + \mathcal{F}_{rlx}(a, l, \kappa) \\ \text{with } \mathcal{F}_{rlx}(a, l, \kappa) &= \int_{\Omega_0} l(a - \kappa) \, d\Omega_0 + \int_{\Omega_0} \frac{r}{2} (a - \kappa)^2 \, d\Omega_0. \end{aligned} \quad (51)$$

A close relation with micromorphic models<sup>27</sup> can be noticed, except for the Lagrangian term. Indeed,  $\kappa$  plays the role of the micromorphic counterpart of the variable  $a$ . But here, an equality between both variables is (weakly) enforced. The evolution of the new variables  $a$  and  $l$  results from the fact that they do not contribute to the dissipation. The latter retains its usual definition:

$$\begin{aligned}
\mathcal{D} = \int_{\Omega_0} \mathbf{T} : \dot{\mathbf{E}} \, d\Omega_0 - \dot{\mathcal{L}} &= \int_{\Omega_0} \left( \mathbf{T} - \frac{\partial \Phi^e}{\partial \mathbf{E}^e} \right) : \dot{\mathbf{E}} \, d\Omega_0 \\
+ \int_{\Omega_0} [ -c \nabla a \nabla \dot{a} - (l + r(a - \kappa)) \dot{a} - (a - \kappa) \dot{l} ] \, d\Omega_0 & \\
+ \int_{\Omega_0} \left[ \frac{\partial \Phi^e}{\partial \mathbf{E}^e} : \dot{\mathbf{E}}^P + \left( l + r(a - \kappa) - \frac{\partial \Phi^P}{\partial \kappa} \right) \dot{\kappa} \right] \, d\Omega_0. &
\end{aligned} \tag{52}$$

In the case of a reversible evolution, for which  $\dot{\mathbf{E}}^P = 0$  and  $\dot{\kappa} = 0$ , the dissipation rate  $\mathcal{D}$  remains equal to zero. This provides the stress-strain relation (44) as previously and the additional equations that govern the evolution of  $a$  and  $l$ :

$$\forall \dot{a} \quad \frac{\partial \mathcal{L}}{\partial \dot{a}} \dot{a} = - \int_{\Omega_0} [c \nabla a \nabla \dot{a} + (l + r(a - \kappa)) \dot{a}] \, d\Omega_0 = 0, \tag{53}$$

$$\forall \dot{l} \quad \frac{\partial \mathcal{L}}{\partial \dot{l}} \dot{l} = - \int_{\Omega_0} (a - \kappa) \dot{l} \, d\Omega_0 = 0. \tag{54}$$

The dissipation rate hence reduces to

$$\mathcal{D} = \int_{\Omega_0} \left[ \mathbf{T} : \dot{\mathbf{E}}^P + \left( l + r(a - \kappa) - \frac{\partial \Phi^P}{\partial \kappa} \right) \dot{\kappa} \right] \, d\Omega_0. \tag{55}$$

The driving force associated with the plastic strain is still the stress tensor. Besides, as expected with the decomposition-coordination method, the driving force associated with the hardening variable  $\kappa$  now involves the new variables but no more a nonlocal term, in contrast to (46):

$$A_{r\kappa} = - \frac{\partial \Phi^P}{\partial \kappa} + l + r(a - \kappa). \tag{56}$$

Finally, the evolution of  $\mathbf{E}^P$  and  $\kappa$  are governed by the evolution equations of the local GTN model (11) with the new expression of the driving force (56).

It can be shown that before spatial discretisation, the relaxed problem is equivalent to the original one. Indeed, satisfying (54) implies that  $a = \kappa$  as expected. Moreover, integrating (53) by parts results in

$$\forall \dot{a} \quad - \int_{\partial \Omega_0} (c \nabla a \cdot \mathbf{n}) \dot{a} \, ds + \int_{\Omega_0} [ \operatorname{div}(c \nabla a) - (l + r(a - \kappa)) ] \dot{a} \, d\Omega_0 = 0. \tag{57}$$

This variational formulation corresponds to the following strong form and boundary condition (where  $a = \kappa$ ):

$$\operatorname{div}(c \nabla a) = l \quad ; \quad \nabla a \cdot \mathbf{n} = 0 \quad \text{on } \partial \Omega. \tag{58}$$

Inserting (58) into (56) shows that the relaxed driving force  $A_{r\kappa}$  coincides with the original driving force  $A_{rl}$  defined in (46). This holds also true for the stress-strain relation, the definition of the driving force associated with the plastic strain (the stress tensor), and the boundary condition on the hardening variable. The relaxed problem is indeed equivalent to the original nonlocal one.

Even though both problems are equivalent on a continuum level, this is no more the case after spatial discretisation; here lies the interest of the decomposition-coordination method. Indeed, on one hand, the displacement  $\mathbf{u}$ , the nonlocal instance of the hardening variable  $a$ , and the Lagrange multiplier  $l$  are discretised on the basis of Lagrange shape functions. They correspond to the nodal unknowns of the discretised problem. On the other hand, the strain  $\mathbf{E}$ , the stress  $\mathbf{T}$ , the plastic strain  $\mathbf{E}^P$ , the local instance of the hardening variable  $\kappa$ , and the porosity are sampled at the integration points. The stress and the internal variables  $\mathbf{E}^P$ ,  $\kappa$ , and  $f$  are thus obtained by integration of the constitutive equations at the integration point level. Sections 3.2 and 3.3 detail this integration step while Sections 3.4 and 3.5 are focused on the spatial discretisation by FEs.

### 3.2 | Constitutive integration: solution algorithm at the integration point level

The relaxed problem detailed above gives rise to a set of constitutive equations, which differ from the original nonlocal ones only in the definition of the yield surface, see box 1. The equations hold for each integration point; the history of the strain, the nonlocal instance of the hardening variable, and the Lagrange multiplier are given at this level. To solve this set of ordinary differential equations, a time-discretisation based on a staggered scheme is applied: the plastic strain, the local instance of the hardening variable, and the stress are computed for a given porosity value by means of an implicit Euler scheme. Then, the porosity is updated on the basis of the computed plastic increment through a first-order implicit scheme again.

More precisely, let us denote, respectively,  $q^-$  (or  $q_-$ ),  $q$ , and  $\Delta q$  the value of a quantity at the beginning of the current time step, at the end of the time step, and its increment during the time step. The integration of the constitutive relations can be stated as follows. The input data consist of  $\mathbf{E}$ ,  $a$ ,  $l$ ,  $\mathbf{E}_-^p$ ,  $\kappa^-$ , and  $f_-$ . The discretisation of the equations related to the plastic evolution by the implicit Euler scheme leads to the following algebraic system, the unknown of which are  $\Delta \mathbf{E}^p$  and  $\Delta \kappa$ :

$$\mathbf{T} = \mathbb{E}:(\mathbf{E} - \mathbf{E}_-^p - \Delta \mathbf{E}^p), \quad (59)$$

$$G(\mathbf{T}, T_*, f^-) = \left(\frac{T_{\text{eq}}}{T_*}\right)^2 + 2q_1 f_-^* \cosh\left(\frac{3q_2 T_H}{2T_*}\right) - 1 - (q_1 f_-^*)^2 = 0, \quad (60)$$

$$\Delta \mathbf{E}^p = \frac{\lambda}{J} \frac{\partial T_*}{\partial \mathbf{T}} \quad ; \quad \Delta \kappa = \lambda, \quad (61)$$

$$\lambda \geq 0 \quad ; \quad \widehat{F} \leq 0 \quad ; \quad \lambda \widehat{F} = 0, \quad (62)$$

$$\text{with } \widehat{F}(T_*, \kappa^- + \Delta \kappa) \equiv F(\mathbf{T}, A_{\text{rlx}}(\kappa)) = \frac{T_*}{J} \bar{\sigma}(\kappa^- + \Delta \kappa) + r(a - \kappa) + l. \quad (63)$$

Then, the implicit discretisation of the porosity evolution equation provides

$$\begin{cases} \Delta f_g = (1 - f^- - \Delta f) \text{tr} \Delta \mathbf{E}^p \\ \Delta f = \Delta f_g + \Delta f_n \end{cases}. \quad (64)$$

The latter system is linear with respect to the porosity and does not raise any difficulty:

$$f = \frac{f^- + \text{tr} \Delta \mathbf{E}^p + f_n(\kappa^- + \Delta \kappa) - f_n(\kappa^-)}{1 + \text{tr} \Delta \mathbf{E}^p}. \quad (65)$$

On the contrary, a robust algorithm is required to solve the plastic evolution (59-63). In this section, we restrict temporarily our attention to the case  $T_* \neq 0$  (hence,  $\mathbf{T} \neq 0$ ) and  $q_1 f_-^* < 1$ . First, the elastic trial stress tensor  $\mathbf{T}^e$  is classically introduced:

$$\mathbf{T}^e = \mathbb{E}:(\mathbf{E} - \mathbf{E}_-^p) \quad \Rightarrow \quad \mathbf{T} = \mathbf{T}^e - \mathbb{E}:\Delta \mathbf{E}^p = \mathbf{T}^e - 3K \Delta E_H^p \mathbf{I} - 2\mu \Delta \mathbf{E}_D^p. \quad (66)$$

If the elastic trial lies in the elasticity domain, ie,  $\widehat{F}(T_*^e, \kappa^-) \leq 0$ , then the solution corresponds to the elastic branch characterised by  $\lambda = 0$ . Consider now the case  $\widehat{F}(T_*^e, \kappa^-) > 0$ . The consistency condition (62) and the definition of the threshold function (63) allow expressing the GTN equivalent stress  $T_*$  as a function of the hardening variable increment:

$$\widehat{T}_*(\Delta \kappa) \equiv T_* = J [\bar{\sigma}(\kappa^- + \Delta \kappa) - r(a - \kappa) - l]. \quad (67)$$

Moreover, the differentiation of (60) provides the plastic flow direction:

$$\frac{\partial T_*}{\partial \mathbf{T}} = -\left(\frac{\partial G}{\partial T_*}\right)^{-1} \left(\frac{\partial G}{\partial \mathbf{T}}\right) = \Theta\left(\frac{T_H}{T_*}, \frac{T_{eq}}{T_*}\right) \left[\frac{3\mathbf{T}_D}{2T_*} + \Lambda\left(\frac{T_H}{T_*}\right)\mathbf{I}\right], \quad (68)$$

where the following notations are introduced to simplify the expressions:

$$\Lambda(x) = \frac{1}{2}q_1q_2f_-^* \sinh\left(\frac{3q_2x}{2}\right), \quad (69)$$

$$\Theta(x, y) = [y^2 + 3x \Lambda(x)]^{-1}. \quad (70)$$

This gives the expression of the mean and deviatoric parts of the plastic strain increment:

$$\Delta E_H^p = \frac{\lambda}{J} \Theta\left(\frac{T_H}{T_*}, \frac{T_{eq}}{T_*}\right) \Lambda\left(\frac{T_H}{T_*}\right) ; \quad \Delta \mathbf{E}_D^p = \frac{3\lambda}{2J} \Theta\left(\frac{T_H}{T_*}, \frac{T_{eq}}{T_*}\right) \frac{\mathbf{T}_D}{T_*}. \quad (71)$$

Substituting the former expressions into the stress-strain relation (59) results in

$$\frac{T_H^e - T_H}{3K} = \frac{\lambda}{J} \Theta\left(\frac{T_H}{T_*}, \frac{T_{eq}}{T_*}\right) \Lambda\left(\frac{T_H}{T_*}\right) ; \quad \mathbf{T}_D = \left[1 + 3\mu \frac{\lambda}{J} \Theta\left(\frac{T_H}{T_*}, \frac{T_{eq}}{T_*}\right) \frac{1}{T_*}\right]^{-1} \mathbf{T}_D^e. \quad (72)$$

The second equation provides the direction of the stress deviator. Besides,  $\Theta$  may be eliminated so that  $T_{eq}$  can be expressed as a function of  $T_H$  and  $\Delta\kappa$ :

$$T_{eq} = T_{eq}^e \left[1 + \frac{\mu}{K} \frac{T_H^e - T_H}{\widehat{T}_*(\Delta\kappa) \Lambda\left(\frac{T_H}{\widehat{T}_*(\Delta\kappa)}\right)}\right]^{-1} \equiv \widehat{T}_{eq}(T_H, \Delta\kappa). \quad (73)$$

After gathering the equations 67, 71, 72, and 73, the initial algebraic system reduces to

$$\begin{cases} \widehat{G}(T_H, \Delta\kappa) = 0 \\ \widehat{\lambda}(T_H, \Delta\kappa) - \Delta\kappa = 0 \end{cases}, \quad (74)$$

with

$$\widehat{G}(T_H, \Delta\kappa) = \frac{\widehat{T}_{eq}(T_H, \Delta\kappa)}{\widehat{T}_*(\Delta\kappa)} \left(\frac{\widehat{T}_{eq}(T_H, \Delta\kappa)}{\widehat{T}_*(\Delta\kappa)}\right)^2 + 2q_1f_-^* \cosh\left(\frac{3q_2}{2} \frac{T_H}{\widehat{T}_*(\Delta\kappa)}\right) - 1 - (q_1f_-^*)^2, \quad (75)$$

$$\widehat{\lambda}(T_H, \Delta\kappa) = J \frac{T_H^e - T_H}{3K \Lambda\left(\frac{T_H}{T_*}\right)} \left[\frac{\widehat{T}_{eq}(T_H, \Delta\kappa)}{\widehat{T}_*(\Delta\kappa)} \left(\frac{\widehat{T}_{eq}(T_H, \Delta\kappa)}{\widehat{T}_*(\Delta\kappa)}\right)^2 + 3 \frac{T_H}{\widehat{T}_*(\Delta\kappa)} \Lambda\left(\frac{T_H}{\widehat{T}_*(\Delta\kappa)}\right)\right]. \quad (76)$$

The nonlinear system (74) is solved by means of an iterative nested algorithm. The inner loop provides  $T_H$  for a given iterate  $\Delta\kappa$  by solving the equation (74)<sub>1</sub>; The result of this inner iterative process is denoted  $\widehat{T}_H(\Delta\kappa)$ . The outer loop consists in finding  $\Delta\kappa$  as the root of the equation (74)<sub>2</sub>. The robustness and the efficiency of the algorithm relies on deriving admissibility intervals for both unknowns. Regarding  $T_H$ , the positivity of  $\lambda$  required by (62) limits the admissible range when considering (76). Indeed,  $\Lambda$  is an odd function and  $x\Lambda(x) \geq 0$  for any value  $x$  so that  $T_H$  and  $T_H^e - T_H$  should have the same sign. Therefore,

$$\begin{cases} \text{if } T_H^e \geq 0 & 0 \leq T_H \leq T_H^e \\ \text{if } T_H^e < 0 & T_H^e \leq T_H \leq 0. \end{cases} \quad (77)$$

We can now show that (74)<sub>1</sub> admits a unique solution  $\widehat{T}_H(\Delta\kappa)$ . Consider  $\Delta\kappa$  so that  $\widehat{T}_*(\Delta\kappa) > 0$  and  $\widehat{T}_*(\Delta\kappa) \leq T_*^e$ . The former inequality is consistent with the assumption of the present section, that is,  $T_* > 0$ . The latter inequality is a general property of the return-mapping algorithm; it will be demonstrated in the next section with a focus on the bounds for  $\Delta\kappa$ . For any  $\Delta\kappa$  that fulfils both inequalities, it can be noticed that

$$\widehat{G}(0, \Delta\kappa) = -(1 - q_1 f_-^*)^2 < 0, \quad (78)$$

$$\widehat{G}(T_H^e, \Delta\kappa) = G(\mathbf{T}^e, \widehat{T}_*(\Delta\kappa), f_-^*) \geq G(\mathbf{T}^e, T_*^e, f_-^*) = 0. \quad (79)$$

In addition,  $\widehat{G}(T_H, \Delta\kappa)$  is a strictly monotonic function with respect to  $T_H$  in the interval (77), increasing if  $T_H^e \geq 0$  and decreasing if  $T_H^e \leq 0$ . Therefore, the equation (74)<sub>1</sub> admits a unique solution  $\widehat{T}_H(\Delta\kappa)$  in the interval (77).

This concludes the presentation of the algorithm used to solve the nonlinear algebraic system resulting from the integration of the constitutive relations in regular cases ( $T_* \neq 0$ ). The existence and uniqueness of the solution  $\Delta\kappa$  to (74)<sub>2</sub> is demonstrated in the next section, where the case  $T_* = 0$  is also considered.

### 3.3 | Singular points: generalised flow rule

The solution algorithm described in the previous section relies on the assumption that  $T_* \neq 0$ , an assumption explicitly used in the derivation of the flow rule (61). This assumption holds generally with local models. But here, the elastic domain may reduce to a single point because of the term  $l + ra$  in the yield function (63), or equivalently the term  $\text{div}(c\nabla\kappa)$  in (48), the sign of which is not prescribed nor controlled. In that case, the flow rule can no more be expressed as in (61). The proper extension of the associative flow rule (11) to singular cases is provided by the principle of maximum dissipation, which encompasses (11) as a special case. It states that the driving forces  $(\mathbf{T}, A)$  are admissible, ie,  $F(\mathbf{T}, A) \leq 0$ , and that the evolution  $(\dot{\mathbf{E}}^p, \dot{\kappa})$  fulfils

$$\forall (\mathbf{T}', A') \quad \text{such as } F(\mathbf{T}', A') \leq 0 \quad : \quad (\mathbf{T} - \mathbf{T}') : \dot{\mathbf{E}}^p + (A - A') \dot{\kappa} \geq 0. \quad (80)$$

As  $(\mathbf{T}, A)$  should be admissible and  $T_* \geq 0$ , a necessary condition is  $A \leq \sigma^0$ . In the case  $A < \sigma^0$ , the flow rule (11) holds, and the results of the previous section are valid. Consider now the singular case corresponding to  $A = \sigma^0$ . The admissibility of  $(\mathbf{T}, A)$  implies that  $T_* = 0$ ; hence,  $\mathbf{T} = 0$  (as long as  $q_1 f^* < 1$ ). In that case, (80) reads

$$\forall (\mathbf{T}', A') \quad \text{such as } \frac{N(\mathbf{T}')}{J} + A' - \sigma^0 \leq 0 \quad : \quad \mathbf{T}' : \dot{\mathbf{E}}^p + A' \dot{\kappa} \leq \sigma^0 \dot{\kappa}. \quad (81)$$

It is shown in Zhang<sup>28</sup> that this inequality is fulfilled if and only if

$$\pi_N(\dot{\mathbf{E}}^p) \equiv \sup_{\sigma; N(\sigma) \leq 1} (\sigma : \dot{\mathbf{E}}^p) \leq \frac{\dot{\kappa}}{J}. \quad (82)$$

In the case of the GTN equivalent stress function  $N$  introduced in (16), the support function  $\pi_N$  can be obtained after some calculations: [Correction added on 13 February 2018, after first online publication: the square root in equation (83) has been corrected]

$$\begin{aligned} \pi_N(\dot{\mathbf{E}}^p) &= \frac{2}{q_2} \text{arc cosh}(1 + C^*) |\dot{E}_H^p| + \frac{2}{3} (1 - q_1 f^*) \sqrt{1 - \gamma C^*} \dot{E}_{eq}^p \\ C^* &= -\chi + \sqrt{\chi^2 + \frac{2}{\gamma}(\chi - 1)} \quad ; \quad \chi = 1 + \frac{1}{q_1 f^*} \left( \frac{3 |\dot{E}_H^p|}{q_2 \dot{E}_{eq}^p} \right)^2 \quad ; \quad \gamma = \frac{2 q_1 f^*}{(1 - q_1 f^*)^2}. \end{aligned} \quad (83)$$

In particular, one can notice that  $\pi_N \geq 0$ ,  $\pi_N$  is positive homogeneous of degree 1, and  $\pi_N(\dot{\mathbf{E}}^p) = 0 \Leftrightarrow \dot{\mathbf{E}}^p = 0$ . Finally, the discrete equations corresponding to the singular plastic flow regime are the following:

$$T_* = 0 \Rightarrow \mathbf{T} = 0 \Rightarrow \begin{cases} \Delta E_H^p = T_H^e/3K \\ \Delta \mathbf{E}_D^p = \mathbf{T}_D^e/2\mu \end{cases}, \quad (84)$$

$$A = \sigma^0 \Rightarrow \bar{\sigma}(\kappa^- + \Delta\kappa) = r(a - \kappa) + l, \quad (85)$$

$$\pi_N(\Delta \mathbf{E}^p) \leq \frac{\Delta\kappa}{J}. \quad (86)$$

Besides, the GTN model as introduced in box 1 for a given porosity belongs to the class of generalised standard materials. The algebraic system of equations that results from the discretisation with an implicit Euler scheme can be interpreted as the minimisation of a potential, see Mialon.<sup>29</sup> This allows asserting the existence and the uniqueness of the incremental solution under conditions that are indeed fulfilled with the GTN model: convexity of the yield function  $F$  with respect to  $(\mathbf{T}, A)$ , strict convexity and coercivity of the Helmholtz free energy with respect to  $(\mathbf{E}^p, \kappa)$ . Thus, despite the 3 possible regimes for the constitutive law (zero plastic flow, regular plastic flow, and singular plastic flow), there exists a unique solution. Therefore, we propose to follow the following scheme to integrate the constitutive relation:

1. Compute the solution under the assumption of singular plastic flow and check whether the condition (86) is fulfilled.
2. If (86) is not fulfilled, compute the solution under the assumption of zero plastic flow and check whether  $\widehat{F}(T_*^e, \kappa^-) \leq 0$ .
3. If (86) is not fulfilled and  $\widehat{F}(T_*^e, \kappa^-) > 0$ , then the solution corresponds to a regular plastic flow. It can be obtained as presented in the previous section.

In the last case (regular plastic flow), it is interesting to express the interval of admissible values  $\Delta\kappa$ . First, we can show that necessarily  $T_* \leq T_*^e$ , a general property of return-mapping algorithm. Indeed, thanks to the convexity of the function  $N$  defined in (16), the following inequality holds true:

$$T_*^e = N(\mathbf{T}^e) \geq N(\mathbf{T}) + \frac{\partial N}{\partial \mathbf{T}}(\mathbf{T}) : (\mathbf{T}^e - \mathbf{T}) = T_* + \frac{\lambda}{J} \left( \frac{\partial T_*}{\partial \mathbf{T}} : \mathbb{E} : \frac{\partial T_*}{\partial \mathbf{T}} \right). \quad (87)$$

Thanks to the positive definiteness of  $\mathbb{E}$ , this implies that  $T_* \leq T_*^e$ . According to (67),  $T_* = \widehat{T}_*(\Delta\kappa)$  and  $\widehat{T}_*$  is a strictly increasing function. Hence, the upper bound on  $T_*$  leads to an upper bound on  $\Delta\kappa$ , with  $\widehat{T}_*^{-1}$  the inverse function of  $\widehat{T}_*$  (which is always defined thanks to  $r > 0$ ):

$$\Delta\kappa \leq \Delta\kappa_M \equiv \widehat{T}_*^{-1}(T_*^e). \quad (88)$$

A lower bound  $\Delta\kappa_m$  is provided by 2 conditions. First,  $\Delta\kappa > 0$  because of (61), (62), and the fact that the solution does not correspond to a zero plastic flow (hence,  $\Delta\kappa \neq 0$ ). In addition, the regular plastic flow regime is characterised by  $A < \sigma^0$ ; hence,  $\widehat{T}_*(\Delta, \kappa) > 0$ . As the function  $\widehat{T}_*$  is strictly increasing,  $\Delta\kappa_m$  is

$$\begin{cases} \text{if } \widehat{T}_*(0) \geq 0 & \Delta\kappa_m = 0 \\ \text{if } \widehat{T}_*(0) < 0 & \Delta\kappa_m \text{ is the (positive) root of } \widehat{T}_*. \end{cases} \quad (89)$$

Therefore, for any  $\Delta\kappa$  such as  $\Delta\kappa_m < \Delta\kappa \leq \Delta\kappa_M$ ,  $0 < \widehat{T}_*(\Delta\kappa) \leq T_*^e$ : This is the condition explicitly used in the previous section. As expected, a solution exists in the interval  $]\Delta\kappa_m, \Delta\kappa_M]$  since the values of the function to solve  $\widehat{\lambda}(\Delta\kappa) - \Delta\kappa$  at the bounds of the interval are of opposite signs. Indeed, for the upper bound,  $\widehat{T}_*(\Delta\kappa_M) = T_*^e$  so that  $\widehat{T}_H(\Delta\kappa_M) = T_H^e$  because the inequality in (79) becomes an equality; hence,  $\widehat{\lambda}(\Delta\kappa_M) = 0$  and

$$\widehat{\lambda}(\Delta\kappa_M) - \Delta\kappa_M = -\Delta\kappa_M < 0. \quad (90)$$

Regarding the lower bound, both cases should be analysed. If  $\Delta\kappa_m = 0$ , then

$$\widehat{\lambda}(\Delta\kappa_m) - \Delta\kappa_m = \widehat{\lambda}(\Delta\kappa_m) \geq 0, \quad (91)$$

since  $\widehat{T}_H(\Delta\kappa_m)$  belongs to the interval (77), which has been derived so as to satisfy  $\widehat{\lambda} \geq 0$ . If  $\Delta\kappa_m \neq 0$ , then  $\widehat{T}_*(\Delta\kappa_m) = 0$  by definition (89). Straightforward (but cumbersome) calculations show that in this case,

$$\widehat{\lambda}(\Delta\kappa_m) = J \pi_N(\mathbb{E}^{-1}:\mathbf{T}^e). \quad (92)$$

Because of the fact that the solution does not correspond to a singular plastic flow, (86) is not fulfilled so that

$$\pi_N\left(\mathbb{E}^{-1}:\mathbf{T}^e\right) > \frac{\Delta\kappa_m}{J}, \quad (93)$$

see also (84) and (85). The former inequality allows the conclusion:

$$\widehat{\lambda}(\Delta\kappa_m) - \Delta\kappa_m = J \pi_N(\mathbb{E}^{-1}:\mathbf{T}^e) - \Delta\kappa_m > 0. \quad (94)$$

In both cases of lower bound  $\Delta\kappa_m$ ,  $\widehat{\lambda}(\Delta\kappa_m) - \Delta\kappa_m \geq 0$ .

Finally, on the basis of a staggered scheme for the porosity and the plastic increment, a solution algorithm has been proposed for the nonlocal (relaxed) GTN constitutive equations. It allows the computation of the unique solution in a robust way, since it relies on the solution of scalar equations with controlled bounds and unique solution. Note that similar solution approaches can be found in the work of Enakoutsa and Leblond,<sup>7</sup> where the authors use different iteration variables and are also able to prove the solution uniqueness. At last, for the sake of completeness, the corresponding consistent tangent matrices are expressed in the Appendices A3 (regular plastic flow regime) and A4 (singular plastic flow regime).

### 3.4 | Finite element formulation

In Sections 3.2 and 3.3, the integration of the constitutive relation has been detailed in the case of the relaxed formulation described in Section 3.1. It is based on the assumption that the Lagrange multiplier  $l$  and the nonlocal instance of the hardening variable  $a$  are given at this stage, in addition to the strain  $\mathbf{E}(\mathbf{u})$ . Let us denote  $\widehat{\mathbf{T}}(\mathbf{E}, a, l)$  and  $\widehat{\kappa}(\mathbf{E}, a, l)$  the result of the constitutive integration. Then the principal unknown  $(\mathbf{u}, a, l)$  are governed by the 3 variational equations (5), (53), and (54), that is,

$$\left\{ \begin{array}{l} \forall \delta \mathbf{u} \quad \delta_u \mathcal{L} = \int_{\Omega_0} \widehat{\mathbf{T}}(\mathbf{E}(\mathbf{u}), a, l) : \delta \mathbf{E} \, d\Omega_0 = \delta \mathcal{W}_{ext} \\ \forall \delta a \quad \delta_a \mathcal{L} = \int_{\Omega_0} [c \nabla a \nabla \delta a + (l + ra) \delta a - r \widehat{\kappa}(\mathbf{E}(\mathbf{u}), a, l) \delta a] \, d\Omega_0 = 0 \\ \forall \delta l \quad \delta_l \mathcal{L} = \int_{\Omega_0} (a - \widehat{\kappa}(\mathbf{E}(\mathbf{u}), a, l)) \delta l \, d\Omega_0 = 0. \end{array} \right. \quad (95)$$

A spatial discretisation by FEs is introduced for these unknowns where  $\underline{\mathbf{N}}^u \in \mathbb{R}^{n \times dim}$ ,  $\underline{\mathbf{N}}^a \in \mathbb{R}^n$ , and  $\underline{\mathbf{N}}^l \in \mathbb{R}^n$  are arrays of Lagrange polynomial basis functions,  $\underline{\underline{\mathbf{B}}}^u \in \mathbb{R}^{dim} \times \mathbb{R}^{dim} \times \mathbb{R}^{n \times dim}$  and  $\underline{\underline{\mathbf{B}}}^a \in \mathbb{R}^{dim} \times \mathbb{R}^{n \times dim}$  are the spatial derivatives of  $\underline{\mathbf{N}}^u$  and  $\underline{\mathbf{N}}^a$ ,  $\underline{\mathbf{U}} \in \mathbb{R}^{n \times dim}$ ,  $\underline{\mathbf{A}} \in \mathbb{R}^n$ , and  $\underline{\mathbf{L}} \in \mathbb{R}^n$  are the arrays of nodal unknowns,  $n$  the number of nodes, and  $dim$  the space dimension:



$$\begin{aligned}\mathbf{u}(\mathbf{x}) &= \underline{\underline{\mathbf{N}}}^u(\mathbf{x}) \cdot \underline{\underline{\mathbf{U}}} \quad ; \quad a(\mathbf{x}) = \underline{\underline{\mathbf{N}}}^a(\mathbf{x}) \cdot \underline{\underline{\mathbf{A}}} \quad ; \quad l(\mathbf{x}) = \underline{\underline{\mathbf{N}}}^l(\mathbf{x}) \cdot \underline{\underline{\mathbf{L}}} \\ \nabla \mathbf{u}(\mathbf{x}) &= \underline{\underline{\mathbf{B}}}^u(\mathbf{x}) \cdot \underline{\underline{\mathbf{U}}} \quad ; \quad \nabla a(\mathbf{x}) = \underline{\underline{\mathbf{B}}}^a(\mathbf{x}) \cdot \underline{\underline{\mathbf{A}}}.\end{aligned}\tag{96}$$

In this work,  $\underline{\underline{\mathbf{N}}}^u$  is piecewise quadratic while  $\underline{\underline{\mathbf{N}}}^a$  and  $\underline{\underline{\mathbf{N}}}^l$  are piecewise linear. As a result, the FE associated with the 3 variables ( $\underline{\underline{\mathbf{U}}}$ ,  $\underline{\underline{\mathbf{A}}}$ ,  $\underline{\underline{\mathbf{L}}}$ ) is a P2P1P1-type element, where P2 stands for quadratic interpolation and P1 stands for linear interpolation, see Figure 1. After spatial discretisation, the variational equations (96) result in the following nonlinear algebraic system, where  $\underline{\underline{\mathbf{R}}}$  corresponds to residuals and  $\underline{\underline{\mathbf{F}}}_{ext}$  denotes the nodal vector of the external load ( $\delta \mathcal{W}_{ext} = \underline{\underline{\mathbf{F}}}_{ext} \cdot \delta \underline{\underline{\mathbf{U}}}$ ):

$$\begin{cases} \underline{\underline{\mathbf{R}}}^u \equiv \sum_g w_g \mathbf{T}_g : \mathbb{P}_g : \left( \mathbf{F}_g^T \cdot \underline{\underline{\mathbf{B}}}^u \right) - \underline{\underline{\mathbf{F}}}_{ext} = 0 \\ \underline{\underline{\mathbf{R}}}^a \equiv \sum_g w_g \left[ (r(a_g - \kappa_g) + l_g) \underline{\underline{\mathbf{N}}}^a + w_g c \nabla a_g \cdot \underline{\underline{\mathbf{B}}}^a \right] = 0 \\ \underline{\underline{\mathbf{R}}}^l \equiv \sum_g w_g (a_g - \kappa_g) \underline{\underline{\mathbf{N}}}^l = 0. \end{cases}\tag{97}$$

The integrals have been approximated in each element by a Gaussian quadrature rule where the index  $g$  refers to a given integration point and  $w_g$  denotes its weight. The unknowns at the Gauss points are obtained by interpolation:

$$\mathbf{F}_g = \mathbf{I} + \underline{\underline{\mathbf{B}}}^u \cdot \underline{\underline{\mathbf{U}}} \quad ; \quad \mathbf{E}_g = \frac{1}{2} \ln \left( \mathbf{F}_g^T \mathbf{F}_g \right) \quad ; \quad a_g = \underline{\underline{\mathbf{N}}}^a \cdot \underline{\underline{\mathbf{A}}} \quad ; \quad \nabla a_g = \underline{\underline{\mathbf{B}}}^a \cdot \underline{\underline{\mathbf{A}}} \quad ; \quad l_g = \underline{\underline{\mathbf{N}}}^l \cdot \underline{\underline{\mathbf{L}}}.\tag{98}$$

The stress and the local instance of the hardening variable are obtained by integration of the constitutive law at each Gauss point:

$$\mathbf{T}_g = \widehat{\mathbf{T}}(\mathbf{E}_g, a_g, l_g) \quad ; \quad \kappa_g = \widehat{\kappa}(\mathbf{E}_g, a_g, l_g).\tag{99}$$

The system (97) is solved classically by an iterative Newton-Raphson method with respect to the nodal unknowns ( $\underline{\underline{\mathbf{U}}}$ ,  $\underline{\underline{\mathbf{A}}}$ ,  $\underline{\underline{\mathbf{L}}}$ ). The expression of the elementary stiffness matrices can be found in Appendix.

### 3.5 | Locking-free element

Volumetric locking is another issue often observed in ductile damage simulation. It arises from plastic quasi-incompressibility in the early stage of damage and leads to strong oscillations in the stress field and interferes with convergence. This is because traditional FEs are not able to account for the incompressibility kinematic relation while preserving enough degrees of freedom at the same time.<sup>26</sup> Some enhanced elements have been developed over the last years and perform well in quasi-incompressible situations, at least in the case of infinitesimal strain. Al-Akhrass et al<sup>16</sup> proposed a Hu-Washizu type mixed FE<sup>30,31</sup> where the volume variation  $\theta$  and the pressure  $P$  are introduced as 2 additional variables. With this relaxed kinematic formulation, deformation and the strain tensors are defined on the basis of a deviatoric/volumetric split as follows:

$$\mathbf{F}(\mathbf{u}, \theta) \equiv \left( \frac{\exp \theta}{J} \right)^{\frac{1}{3}} \mathbf{F} \quad ; \quad \widetilde{\mathbf{E}}(\mathbf{u}, \theta) \equiv \frac{1}{2} \ln \left( \widetilde{\mathbf{F}}^T \cdot \widetilde{\mathbf{F}} \right) = \mathbf{E} + \frac{1}{3} (\theta - \text{tr} \mathbf{E}) \mathbf{I},\tag{100}$$

and the pressure variable  $P$  plays the role of a Lagrange multiplier to weakly ensure the relation  $\theta = \text{tr} \mathbf{E}$ . The Helmholtz free energy is relaxed again by incorporating the new variables  $(\theta, P)$  and the control term  $\mathcal{F}_{inco}$  into the former expression (51):

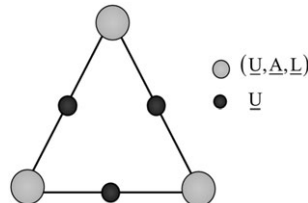


**FIGURE 1** Triangle element for the nonlocal formulation

$$\begin{aligned} \mathcal{L}(\mathbf{u}, \theta, P, a, l, \kappa, \mathbf{E}^P) &= \mathcal{F}_{loc}(\tilde{\mathbf{E}}(\mathbf{u}, \theta), \mathbf{E}^P, \kappa) + \mathcal{F}_{inco}(\mathbf{u}, \theta, P) + \mathcal{F}_{gdt}(a) + \mathcal{F}_{rx}(a, l, \kappa) \\ &\text{with } \mathcal{F}_{inco}(\mathbf{u}, \theta, P) = \int_{\Omega_0} P(\text{tr}\mathbf{E} - \theta) d\Omega_0. \end{aligned} \quad (101)$$

Now, the saddle-point  $(\mathbf{u}, \theta, P, a, l)$  of this Lagrangian is characterised by the following variational equations, where the integration of the constitutive relation has been introduced:

$$\left\{ \begin{array}{l} \forall \delta \mathbf{u} \quad \delta_{\mathbf{u}} \mathcal{L} = \int_{\Omega_0} [\hat{\mathbf{T}}_D(\tilde{\mathbf{E}}(\mathbf{u}, \theta), a, l) + P \mathbf{I}] : \delta \mathbf{E} d\Omega_0 = \delta \mathcal{W}_{ext} \\ \forall \delta \theta \quad \delta_{\theta} \mathcal{L} = \int_{\Omega_0} [\hat{T}_H(\tilde{\mathbf{E}}(\mathbf{u}, \theta), a, l) - P] \delta \theta d\Omega_0 = 0 \\ \forall \delta P \quad \delta_P \mathcal{L} = \int_{\Omega_0} [\text{tr}\mathbf{E} - \theta] \delta P d\Omega_0 = 0 \\ \forall \delta a \quad \delta_a \mathcal{L} = \int_{\Omega_0} [c \nabla a \nabla \delta a + (l + r a) \delta a - r \hat{\kappa}(\tilde{\mathbf{E}}(\mathbf{u}, \theta), a, l) \delta a] d\Omega_0 = 0 \\ \forall \delta l \quad \delta_l \mathcal{L} = \int_{\Omega_0} (a - \hat{\kappa}(\tilde{\mathbf{E}}(\mathbf{u}, \theta), a, l)) \delta l d\Omega_0 = 0 \end{array} \right. \quad (102)$$

Compared to (95), it can be noticed that the constitutive relation now depends on the relaxed strain tensor  $\tilde{\mathbf{E}}$  instead of the original one  $\mathbf{E}$ . Nevertheless, the problem (102) is equivalent to (95) since (102)<sub>3</sub> results in  $\theta = \text{tr}\mathbf{E}$  while (102)<sub>2</sub> leads to  $P = T_H$ . The interest of the relaxation appears when discretising the variational formulation by FEs.

The spatial discretisation for the variables  $(\mathbf{u}, a, l)$  is the same as previously in (96). The new variables  $(\theta, P)$  are also discretised on the basis of Lagrange shape functions  $\underline{\mathbf{N}}^\theta \in \mathbb{R}^n$  and  $\underline{\mathbf{N}}^P \in \mathbb{R}^n$ , resulting in the arrays of nodal unknowns  $\underline{\Theta} \in \mathbb{R}^n$  and  $\underline{P} \in \mathbb{R}^n$ :

$$\theta(\mathbf{x}) = \underline{\mathbf{N}}^\theta(\mathbf{x}) \cdot \underline{\Theta} \quad ; \quad P(\mathbf{x}) = \underline{\mathbf{N}}^P(\mathbf{x}) \cdot \underline{P}. \quad (103)$$

In this work,  $\underline{\mathbf{N}}^\theta$  and  $\underline{\mathbf{N}}^P$  are piecewise linear interpolation function. The FE associated with the 5 variables  $(\underline{\mathbf{U}}, \underline{\Theta}, \underline{P}, \underline{A}, \underline{L})$  is a P2P1P1P1P1-type element, see Figure 2. The formulation for incompressibility treatment is directly based on the Taylor-Hood element, which is known to fulfil the LBB condition.<sup>32</sup> A linear interpolation for  $a$  is chosen to be “consistent” with the linear strain field.

After spatial discretisation, the variational equations 102 result in the following nonlinear algebraic system:

$$\left\{ \begin{array}{l} \underline{\mathbf{R}}^u \equiv \sum_g w_g (\mathbf{T}_{Dg} + P_g \mathbf{I}) : \mathbf{P}_g : \left( \mathbf{F}_g^T \cdot \underline{\underline{\mathbf{B}}}_g^u \right) - \underline{\mathbf{F}}_{ext} = 0 \\ \underline{\mathbf{R}}^\theta \equiv \sum_g w_g (T_{Hg} - P_g) \underline{\mathbf{N}}_g^\theta = 0 \\ \underline{\mathbf{R}}^P \equiv \sum_g w_g (\text{tr}\mathbf{E}_g - \theta_g) \underline{\mathbf{N}}_g^\theta = 0 \\ \underline{\mathbf{R}}^a \equiv \sum_g w_g \left[ (r(a_g - \kappa_g) + l_g) \underline{\mathbf{N}}_g^a + w_g c \nabla a_g \cdot \underline{\underline{\mathbf{B}}}_g^a \right] = 0 \\ \underline{\mathbf{R}}^l \equiv \sum_g w_g (a_g - \kappa_g) \underline{\mathbf{N}}_g^l = 0. \end{array} \right. \quad (104)$$

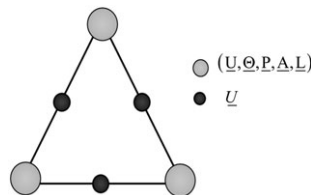


**FIGURE 2** Five-field locking-free element in the nonlocal model

The stress and the local instance of the hardening variable are obtained by integration of the constitutive law at each Gauss point:

$$\tilde{\mathbf{T}}_g = \hat{\mathbf{T}}(\tilde{\mathbf{E}}_g, a_g, l_g) \quad ; \quad \tilde{\kappa}_g = \hat{\kappa}(\tilde{\mathbf{E}}_g, a_g, l_g), \quad (105)$$

where the tilde is introduced as a reminder to the fact that the constitutive law now depends on the relaxed strain  $\tilde{\mathbf{E}}$ . The system (104) is solved classically by an iterative Newton-Raphson method with respect to the nodal unknowns  $(\underline{\mathbf{U}}, \underline{\mathbf{Q}}, \underline{\mathbf{P}}, \underline{\mathbf{A}}, \underline{\mathbf{L}})$ . The expression of the elementary stiffness matrices can be found in Appendix. It can be noticed that the volume variation  $\theta$  could be eliminated in the case of J2 plasticity since it is then proportional to the pressure  $P$  (the plasticity nonlinearity only involves the deviatoric terms). This is no more the case with the GTN constitutive relation where the hydrostatic and deviatoric terms are coupled. Therefore, the volume variation  $\theta$  keeps its status of independent variable.

Even though the efficiency of such mixed FEs with respect to the volumetric locking has been shown in the literature for infinitesimal strain problems, see again Taylor,<sup>17</sup> for instance, it has been observed in Lorentz<sup>12</sup> and Auricchio et al<sup>33</sup> that spurious (ie, purely numerical) plastic localisation bands may occur in finite strain simulations with  $(\underline{\mathbf{U}}, \underline{\mathbf{P}})$  an  $(\underline{\mathbf{U}}, \underline{\mathbf{Q}}, \underline{\mathbf{P}})$  mixed FEs. Here, thanks to the regularisation brought by the introduction of the nonlocal term in  $\nabla a$ , such spurious localisation seems to be precluded, as checked in the numerous computations performed in Zhang.<sup>28</sup> The 5-field mixed FE introduced here hence appears as an adequate choice to deal with volumetric locking and damage localisation that appear in ductile material simulations. The physical relevance of the present formulation in association with the GTN constitutive law is studied in the next section through several comparisons with experimental results.

## 4 | APPLICATION AND SIMULATION

In the frame of the European project STYLE (structural integrity for lifetime management), fracture tests were performed on several specimens. This includes various notched axisymmetric tensile bars (NT), compact tension (CT), and single edge notched tensile (SENT) precracked specimens. The geometries of the specimens are presented in Appendix together with the corresponding FE meshes. In this section, attention is first focused on the role of model parameters on fracture prediction. Then the parameters are identified according to fracture tests on NT4 and CT20 specimens. Finally, simulations using the identified parameters are confronted to the experimental observations for the entire set of specimens.

### 4.1 | Parametric study

In this part, a parametric study using a NT4 specimen (see Appendix Figure A1 for the geometry and meshes) is performed to show the impact of some important parameters of the model on fracture predictions. This kind of study will be helpful for parameter identification when it comes to compare simulation with experiments. In the GTN model, 3 sets of parameters can be distinguished (see Table 1). The first one deals with the description of plasticity, the second with damage, and the last one with the nonlocal model formulation.

In this study, an exponential function is adopted to describe the hardening law:

$$\bar{\sigma}(\kappa) = \sigma^0 + A_1(1 - e^{-B_1\kappa}) + A_2(1 - e^{-B_2\kappa}). \quad (106)$$

Focus is paid on the nonlocal and damage parameters. The initial porosity can be determined from material micrographs or chemical composition. In the following simulations, its value is fixed to  $f_0 = 0.0002$ , which is estimated according to the chemical composition of the studied steel. Then  $q_1$  is fixed at its usual value 1.5, same as what is used in Besson et al.<sup>20</sup> As mentioned before,  $\frac{r}{2}(a - \kappa)^2$  is a penalty term in the nonlocal Lagrangian to force  $a$  to be close to  $\kappa$ . Its role is hence purely numerical to preclude micro instabilities. The penalty parameter  $r$  should not be too small to control the difference between the local instance and nonlocal instance of hardening variable. On the other hand, it cannot be too large either because that may considerably slacken convergence rate during the computation. Usually, one takes a value between  $[10\sigma_0, E]$ .

**TABLE 1** Parameters in a complete nonlocal Gurson-Tvergaard-Needleman (GTN) model

Plasticity parameters	$E$	Young modulus
	$\nu$	Poisson coefficient
	$\sigma_0$	Yield stress
	$A_1, A_2, B_1, B_2$	Hardening parameters
Damage parameters	$f_0$	Initial porosity
	$q_1, q_2$	GTN parameters
	$f_c$	Coalescence porosity
	$\delta$	Acceleration coefficient
	$f_N, p_N, s_N$	Nucleation parameters
Nonlocal parameters	$c$	Nonlocal parameter
	$r$	Penalty parameter

The role of the other parameters will be studied here. In the absence of contrary indications, the parameters take the default values as follows:

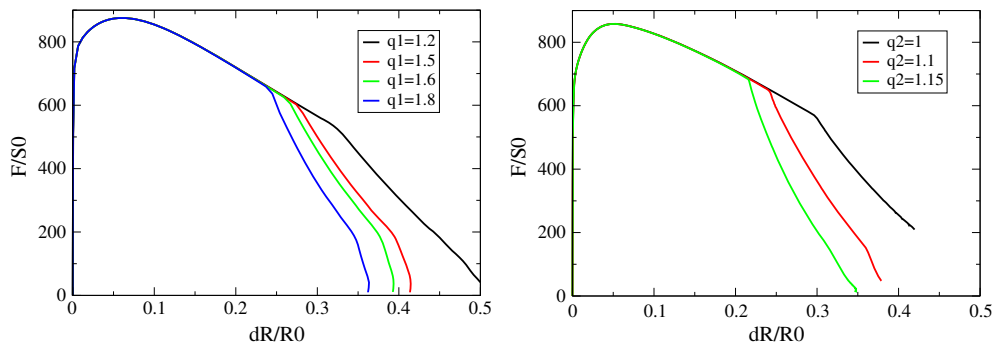
$$\begin{aligned}
 E &= 190000\text{MPa}; \quad \nu = 0.3; \quad \sigma_0 = 488\text{MPa} \\
 R(\kappa) &= 488 + 57 \times (1 - e^{-8613\kappa}) + 239 \times (1 - e^{-10\kappa}) \\
 f_0 &= 2 \times 10^{-4}; \quad f_c = 5 \times 10^{-2}; \quad f_N = 0 \\
 q_1 &= 1.5; \quad q_2 = 1; \quad \delta = 1 \\
 c &= 0\text{N}; \quad r = 5000\text{MPa}
 \end{aligned} \tag{107}$$

In the following, the normalised force  $F/S_0$ (MPa) vs diameter reduction  $\Delta R/R_0$  curves will be examined for the NT4 geometry type. These curves exhibit a sharp load drop, which corresponds to crack initiation at the centre of the specimen and subsequent crack propagation.

Simulations show that the “fracture point” (ie, the point where the sharp load drop begins) strongly depends on the values of  $q_1$  and  $q_2$ . The higher their values, the earlier the fracture takes place, cf Figure 3.

Figure 4 presents impact of  $\delta$  on simulation results for 2 different coalescence porosities  $f_c = 0.05$  and  $f_c = 0.001$ , respectively. It can be observed that at a low  $f_c = 0.001$ , both the fracture point and the “fracture slope,” which corresponds to fracture propagation rate, depend on  $\delta$ : Larger  $\delta$  gives earlier fracture point and steeper fracture slope. However, it appears that for a high value for  $f_c = 0.05$ , the fracture point is no longer sensible to  $\delta$  while the fracture slope is still influenced by  $\delta$ .

Various values of  $c$  were also used in the simulation to study its influence on the force-displacement curve. As is shown in Figure 5,  $c$  has very little impact on the hardening stage but plays a role during crack propagation in the NT4 specimen. High values of  $c$  tend to delay fracture initiation, which eventually almost disappears (see  $c = 25\text{N}$  in Figure 5). For  $c = 1\text{N}$ , the mesh size ( $60 \mu\text{m}$  at damaged zone) is enough to obtained converged results so that the same is true for  $c = 4\text{N}$  and  $c = 25\text{N}$ .

**FIGURE 3** Force-diameter reduction curves for an NT4 specimen with various values for  $q_1$  and  $q_2$

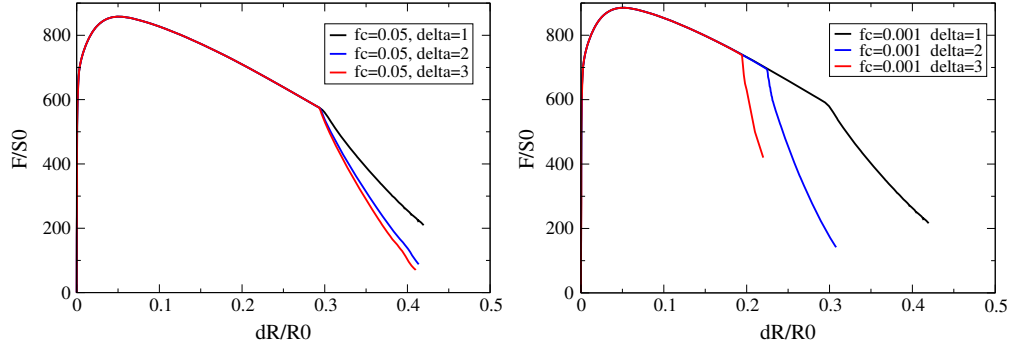


**FIGURE 4** Force-diameter reduction curves for an NT4 specimen with various values for  $f_c$ . Left,  $f_c = 0.05$ ; right,  $f_c = 0.001$

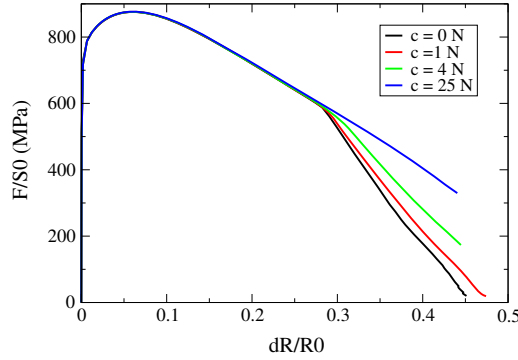


**FIGURE 5** Force-diameter reduction curves for NT4 specimen with various values for  $c$

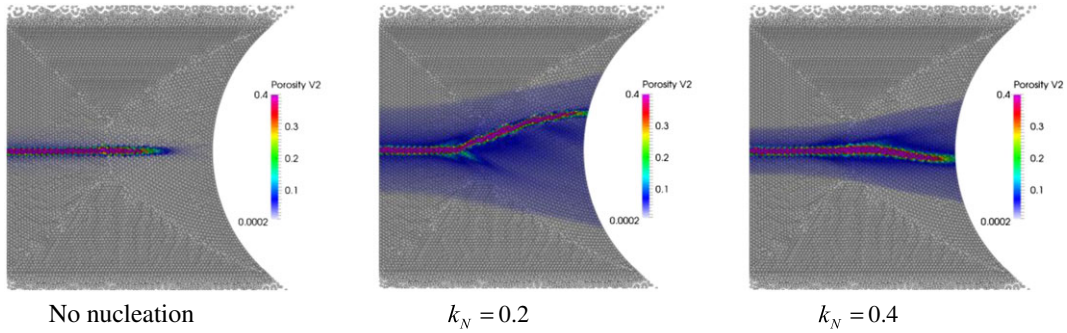


**FIGURE 6** Effect of damage nucleation on crack propagation in an NT4 specimen (values at Gauss points are shown in the undeformed configuration)

The role of nucleation is studied in Figure 6. Fixed values for  $f_N = 0.018$ ,  $s_N = 0.05$ , and  $c = 1N$  are prescribed while  $\kappa_N = 0.2$  and  $\kappa_N = 0.4$  are used. In absence of nucleation, a flat crack path perpendicular to the main loading direction is obtained. For  $\kappa_N = 0.2$ , a clear cup-cone fracture profile is obtained. For  $\kappa_N = 0.4$ , the effect is less pronounced. Finally, for  $\kappa_N = 0.8$  not shown in Figure 6, cup-cone fracture disappears as fracture by void growth occurs before nucleation can play a role. Note that cup-cone fracture is often observed in the experiments using tensile smooth and notched bars.<sup>34</sup>

## 4.2 | Effect of nonlocal regularisation

The aforementioned regularisation method has been proved efficient to regularise a damage field.<sup>35,36</sup> In case of ductile damage, one should also verify whether the localization of damage is also regularised. Simulations have also been performed on the NT4 specimen with various values of the nonlocal parameter  $c$ , cf Figure 7.

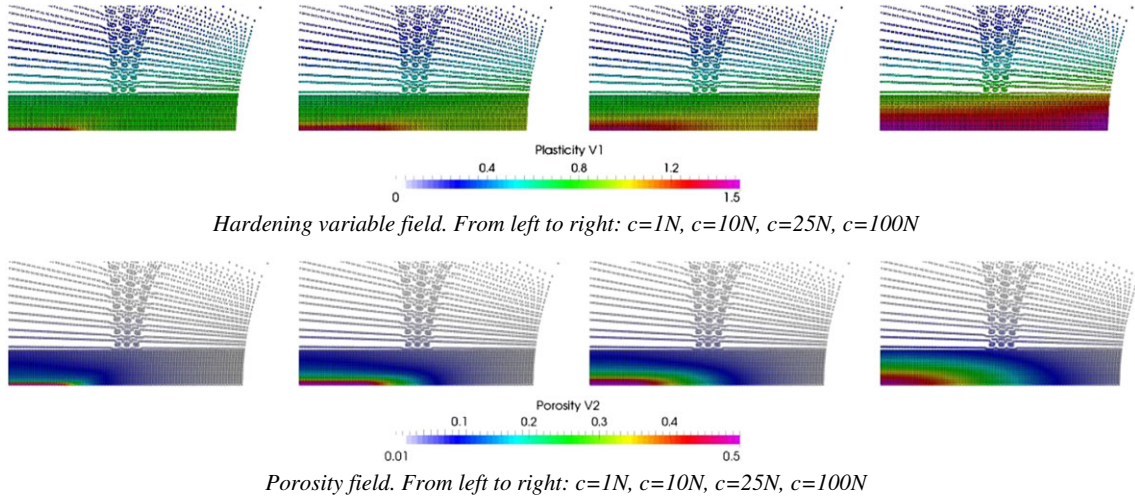


**FIGURE 7** Simulation results for different values of  $c$

It can be observed that the nonlocal parameter  $c$  is able to control the localization bandwidth for both the hardening variable  $\kappa$  and the porosity. It is also important to relate the bandwidth  $l_b$  to the nonlocal parameter. In the following, the band is defined as the zone where porosity is between  $2f_c$  and the fracture porosity  $f_f$ . Several simulations were performed varying both  $c$  and the yield stress  $\sigma_0$ . An empirical relation was deduced from this parametric study, which reads

$$l_b \approx \frac{3}{2} \sqrt{\frac{c}{\sigma_0}}. \quad (108)$$

Note that other nonlocal models use parameters that directly represent a length (see, eg, Huetter et al<sup>37</sup>). In that case, this length does not directly correspond to the bandwidth so that a correlation between these 2 quantities must also be established. In practice, the bandwidth is related to material characteristics such as the average distance between cavities. It can be estimated from microscopic observations. Once the characteristic length is known, one can use (108) to estimate  $c$ .

Nonlocal models become mesh independent when the mesh size is small enough. This property is also verified in this work by simulations with different meshes for a fixed value of  $c$ . For  $c=1N$ , Figure 8 exhibits convergence for a mesh size smaller than  $120 \mu\text{m}$ , which is of the same order as  $3/2\sqrt{c/\sigma_0} \approx 70 \mu\text{m}$ . That implies that equation (108) gives an approximation of a mesh size below which simulation results are mesh independent.

To prove the robustness of the proposed nonlocal formulation, 2 additional meshes were generated. The first one consists of an irregular mesh using triangles (see Figure 9). The second one is intentionally oriented and uses quadrangles. Using the local model, a zigzagging crack is obtained in the first case while an inclined crack following the oriented mesh is obtained in the second case. Using the regular mesh (see Appendix Figure A1), a flat crack is obtained. These results

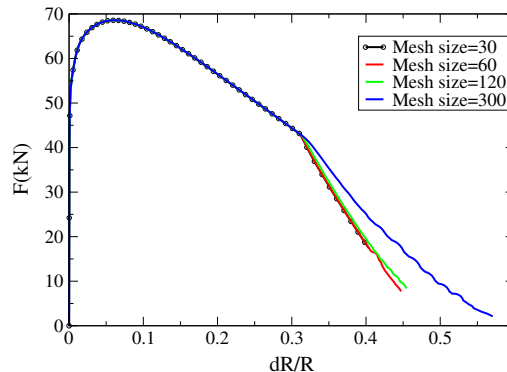


**FIGURE 8** Simulation on NT4 with different mesh size ( $\mu\text{m}$ ). Solution converged



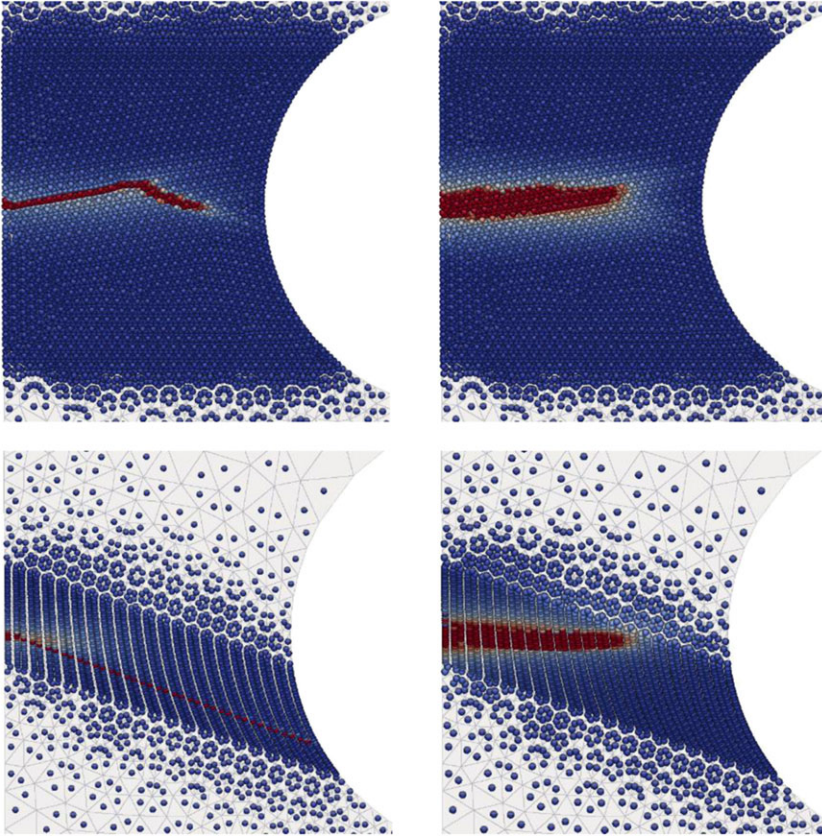


**FIGURE 9** Damage field in an NT4 specimen using an irregular and an intentionally oriented mesh. Left, local. Right, nonlocal (each dot in the figures corresponds to an integration point)

clearly show that the crack path (eg, cup-cone fracture) can be prescribed for a given material model by using an ad hoc mesh in the standard local case. On the other hand, the nonlocal model leads to a reliable result, which does not depend on the FE discretization provided the mesh size is small enough.

### 4.3 | Identification procedure

In this section, parameter identification will be presented in details. As shown in Table 1, there are more than 10 parameters in the proposed nonlocal GTN model. They are identified according to the force-displacement curves obtained from tearing tests of NT4 and CT20 specimens (see Appendix for their geometries and meshes). The following procedure using several fixed parameters is adopted so as to simplify the identification work.

- Simulations are performed with axisymmetric modelling for NT4 specimens and with 3D modelling for CT20 specimens.
- Plasticity parameters are identified using tensile tests on NT specimens NT4. The hardening law is chosen following (106), and an inverse method is used to match the simulated force-displacement curve with the experiment. Due to the low value of the initial porosity, coupling between plasticity and damage may be neglected at this stage.
- Initial porosity  $f_0$  can be determined by microscopic observation or chemical analysis. Some authors, such as, Xue et al<sup>38</sup> and Cao et al<sup>39</sup> consider  $f_0$  as a parameter to be adjusted. Due to lack of microscopic observation in this work, Franklin formula<sup>40</sup> is used to evaluate the volume fraction of MnS inclusions, which easily detach from the matrix so that they can be considered as initial voids. Therefore,  $f_0 = 0.54 \left( \%S - \frac{0.001}{\%Mn} \right)$  is used to estimate the initial porosity.

One obtains  $10^{-4}$  as an order of magnitude, and it is reasonable to set  $f_0 = 2 \times 10^{-4}$ , a value commonly used in some other works<sup>20,41,42</sup> dealing with modern steels.

- Parameter  $q_1$  is fixed to 1.5, and the coalescence porosity is chosen as  $f_c = 0.05$ , which is consistent with results of unit cell calculations by Koplik and Needleman<sup>43</sup> and Shinohara et al.<sup>44</sup>
- Nucleation term in (31) is not used here. As shown before, it can be used to reproduce cup-cone fracture. However, crack initiation in notched bars and crack propagation in precracked specimens is essentially controlled by void

growth and coalescence due to the relative high stress triaxiality. Simulation of notched bars up to cup-cone formation is outside the scope of this work.

- The only remaining damage parameters  $q_2$  and  $\delta$  are fitted according to the force-displacement curve of NT specimens. As mentioned before,  $q_2$  determinates the fracture point and  $\delta$  the fracture slope. Note that the nucleation term favouring the crack propagation is not activated, and slight difference of the fracture slope is tolerated.
- Finally, the value of  $c$  is adjusted based on tests on CT20 specimens in which stable crack propagation takes place. It was checked that the selected mesh size is small enough so that simulations are mesh independent for the adjusted value of  $c$ .

The optimised parameters are gathered in Table 2. Figure 10 compares experiments and simulations for the tests for which parameter determination was performed.

#### 4.4 | Model validation on the entire test database

Specimens not used for parameter fit are simulated using values gathered in Table 2. This includes NT2, NT10, CT12.5, and SENT20 specimens. Geometries and FE meshes are shown in Appendix. Comparison of simulated and experimental force-displacement diagram is presented in Figures 11–13.

Simulations show a rather good agreement between experiments and simulations for all specimens in terms of the force-displacement curves. In the case of CT and SENT specimens, experimental crack propagation was determined using the unloading compliance technique. In simulations, the crack is defined as the zone where porosity is larger than  $2f_c$ . Figure 14 shows crack propagation in a 3D simulation of CT20 specimen. The ASTM-1820 method to define crack propagation (9-point method) is then used to post-process FE simulations so as to compute a mean simulated crack propagation. Figures 15 (CT) and 16 (SENT) compare the experimental and simulated crack mouth opening displacement vs crack propagation curves. A good agreement is obtained in all cases.

**TABLE 2** Identification result of nonlocal Gurson-Tvergaard-Needleman models

Plastic parameters	$E$	$1.9 \times 10^5 \text{MPa}$
	$\nu$	0.3
	Hardening law $R(p)$	$R(p) = 488 + 57 \times (1 - e^{-8613p}) + 239 \times (1 - e^{-10p}) \text{(MPa)}$
Damage parameters	$f_0$	$2 \times 10^{-4}$
	$q_1, q_2$	1.5, 1.07
	$f_c$	0.05
	$\delta$	3
	$f_N, p_N, s_N$	Deactivated term ( $f_N = 0$ )
Nonlocal parameters	$c$	$c = 1\text{N}$ (so that $l_b \approx 70 \mu\text{m}$ )
	$r$	$r = 5000\text{MPa}$

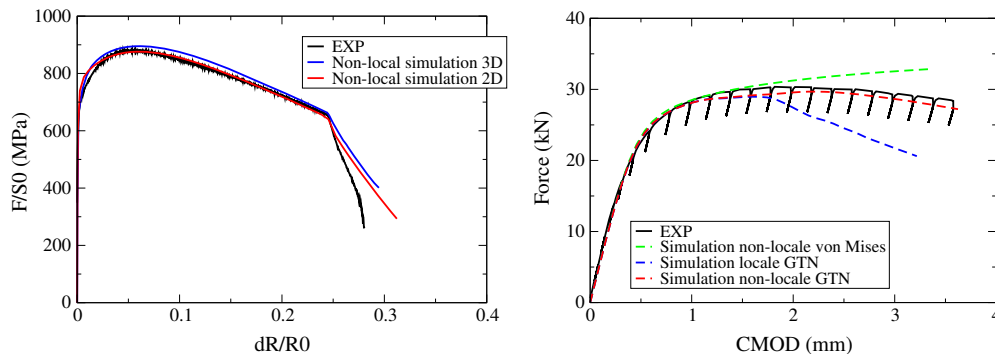


**FIGURE 10** Comparison between simulation and experiments. Left, NT4 specimens. Right, CT20 specimens. CMOD, crack mouth opening displacement; GTN, Gurson-Tvergaard-Needleman



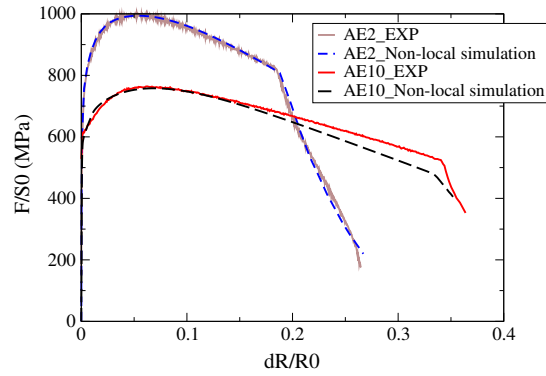


**FIGURE 11** Comparison between the simulation and experiments: NT2 and NT10

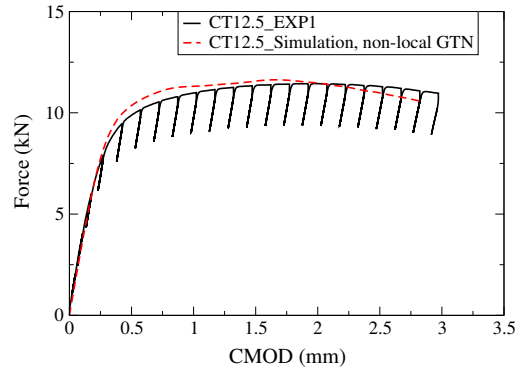


**FIGURE 12** Comparison between the simulation and experiments: CT12.5. CMOD, crack mouth opening displacement; GTN, Gurson-Tvergaard-Needleman

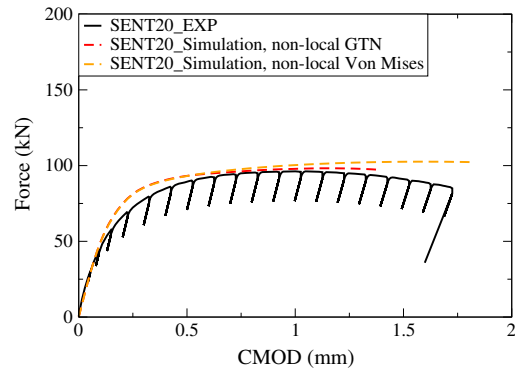


**FIGURE 13** Comparison between the simulation and experiments: SENT20. CMOD, crack mouth opening displacement; GTN, Gurson-Tvergaard-Needleman

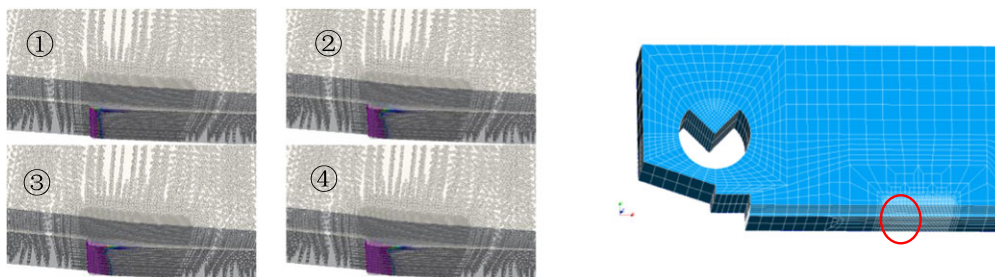


**FIGURE 14** Crack propagation at various load steps in the CT20 specimen, zoom in the circled area

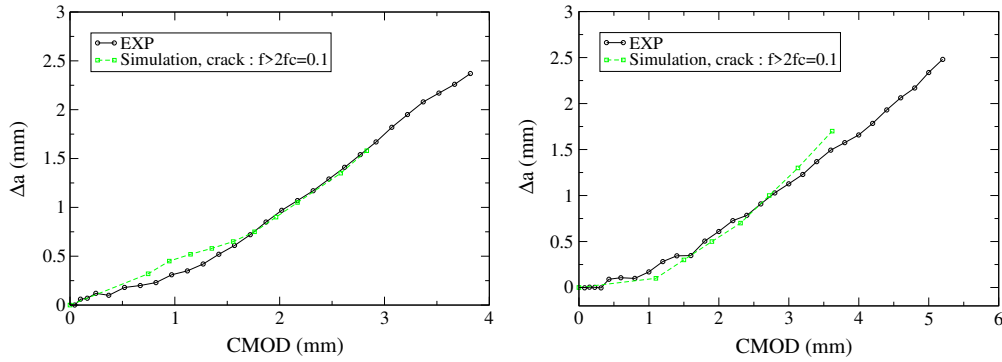


**FIGURE 15** Comparison of crack propagation between the simulation and the experiment: CT12.5 (left) and CT20 (right). CMOD, crack mouth opening displacement

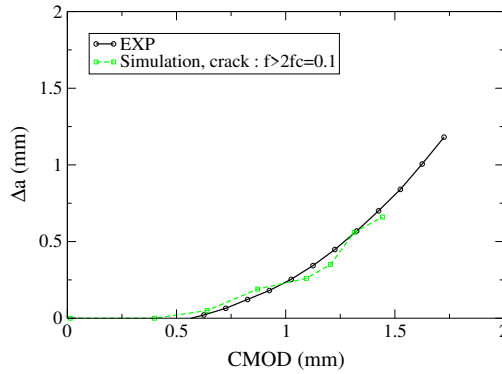


**FIGURE 16** Comparison of crack propagation between the simulation and the experiment: SENT20. CMOD, crack mouth opening displacement

## 5 | SUMMARY

In this work, a locking-free regularised FE formulation is proposed to deal with ductile fracture at large strains. The element is based on a 5-field formulation. The GTN model was adapted to deal with the regularisation technique. Note that many other models for ductile fracture (including more advanced extensions of the Gurson model) could also be used within the proposed FE framework. Algorithm and numerical implementation are detailed. The efficiency of the formulation to deal with mesh dependency is verified. It is demonstrated that the proposed 5-field formulation is robust enough in both 2D and 3D simulations. Mesh independence is verified with respect to mesh size and mesh arrangement.

The proposed computational strategy is applied to an existing database on a nuclear piping steel. The GTN model is calibrated on 2 types of specimens (NT4 and CT20). It is shown that the fitted model is able to reproduce the entire database including force-displacement and crack extension-crack mouth opening displacement curves.

The convergence rate of the simulations is usually very good before the cracks start to propagate. After the onset of crack, cracked elements lose their stiffness and may become extremely distorted. This may strongly reduce the convergence rate of the simulations in particular for long cracks. Further studies will concentrate on the transition from damage to crack to develop a robust algorithm for the propagation stage.

## ACKNOWLEDGEMENTS

This work was supported in part by EDF Lab and in part by the Material Center of Mines ParisTech. Authors acknowledge support from the EDF Lab at Renardières and the European Union project “STYLE” for the experimental databases.

## NOMENCLATURE

. Scalar product

:	Tensor contraction
$\mathbf{I}$	Second-order identity tensor
$X$	A scalar
$\underline{X}$	A vector
$\mathbf{X}$	A second-order tensor
$\times$	A high-order (more than 2) tensor
$\dot{X}$	Evolution rate with respect to time
$X_{nl}$	Nonlocal variable
$\Delta X$	Increment of a variable during a time step
$X^-, \mathbf{X}^-$	Variables of the last time step
$X^+, \mathbf{X}^+$	Variables in the next time step
$X_g, \mathbf{X}_g$	Variables at the Gauss point level
$\mathbf{X}^T$	Transpose of $\mathbf{X}$
$\text{tr}(\mathbf{X})$	Trace of tensor $\mathbf{X}$
$X_H$	Hydrostatic part of tensor $\mathbf{X}$ defined by $X_H = 1/3\text{tr}(\mathbf{X})$
$\text{dev}(\mathbf{X})$ or $\mathbf{X}_D$	Deviator of tensor $\mathbf{X}$ defined by $\text{dev}(\mathbf{X}) = \mathbf{X} - X_H \mathbf{Id}$
$\nabla$	Gradient operator
$\text{div}$	Divergence operator
$A(\kappa)$	Thermodynamic force related to plastic evolution
$a$	Nonlocal hardening variable
$\mathbf{C}$	Cauchy-Green tensor
$c$	Nonlocal model parameter
$D$	Dissipation rate
$\mathcal{D}$	Global dissipation rate
$\mathbf{D}$	Euler deformation rate
$\mathbf{E}$	Logarithmic deformation tensor
$\mathbf{E}^e$	Elastic part of the deformation
$\mathbf{E}^p$	Plastic part of the deformation
$\mathbb{E}$	Elastic stiffness matrix
$\mathbf{F}$	Transformation gradient tensor
$F$	Yield function
$\mathcal{F}$	Helmholtz free energy of the system
$f$	Porosity, void volume fraction of material
$f_c$	Porosity of coalescence
$f_f$	Fracture porosity
$f^*$	Effective porosity
$\dot{f}_g$	Porosity variation rate due to cavity growth
$\dot{f}_n$	Porosity variation rate due to cavity nucleation
$f_{N_i}, p_{N_i}, s_{N_i}$	Void nucleation model parameters
$J$	Jacobian determinant of transformation gradient
$\mathcal{L}$	System Lagrangian
$l$	Lagrange multiplier
$\mathcal{P}_i$	Internal work
$P$	Pressure
$\mathbb{P}$	Fourth-order tensor defined by $\mathbb{P} = 2 \partial \mathbf{E} / \partial \mathbf{C}$
$q_1, q_2$	Gurson model parameters
$r$	Penalization parameter of nonlocal model
$\mathbf{T}$	Work conjugate to the logarithmic deformation tensor
$\mathbf{T}^e$	Elastic trial stress tensor
$T^*$	Effective scalar stress measure associated with $\mathbf{T}$ in Gurson model
$\mathcal{W}_{ext}$	External work
$\delta$	Acceleration factor to describe coalescence

$\kappa$	Hardening variable
$\mu$	Shear module coefficient
$\tilde{\lambda}, \lambda$	Lagrange multiplier
$\mathbf{v}$	$\mathbf{v} = \partial T^*/\partial \mathbf{T}$
$\Omega_0$	Volume in the initial configuration
$\Phi$	Helmholtz free energy
$\Phi^e$	Elastic part of free energy
$\Phi^p$	Plastic part of free energy
$\Psi$	Plastic energy dissipation
$\rho_0$	Density of material in the initial configuration
$\sigma_0$	Yield stress
$\boldsymbol{\sigma}$	Cauchy stress tensor
$\sigma^*$	Effective scalar stress measure associated with $\boldsymbol{\sigma}$ in Gurson model
$\boldsymbol{\tau}$	Kirchhoff stress tensor
$\theta$	Volume variation

## ORCID

Yi Zhang  <http://orcid.org/0000-0003-0428-3960>

Eric Lorentz  <http://orcid.org/0000-0001-6937-6805>

Jacques Besson  <http://orcid.org/0000-0003-1975-2408>

## REFERENCES

- Pardoen T, Scheyvaerts F, Simar A, Tekoğlu C, Onck PR. Multiscale modeling of ductile failure in metallic alloys. *C R Phys.* 2010;11(3–4):326-345.
- Gurson AL. Continuum theory of ductile rupture by void nucleation and growth: part I—yield criteria and flow rules for porous ductile media. *J Eng Mater Technol.* 1977;99(1):2-15.
- Tvergaard V, Needleman A. Analysis of the cup-cone fracture in a round tensile bar. *Acta Metall.* 1984;32(1):157-169.
- Besson J. Continuum models of ductile fracture: a review. *Int J Damage Mech.* 2010;19(1):3-52.
- Benzerga AA, Leblond J-B. Ductile fracture by void growth to coalescence. *Adv Appl Mech.* 2010;44:169-305.
- Springmann M, Kuna M. Identification of material parameters of the Gurson-Tvergaard-Needleman model by combined experimental and numerical techniques. *Comput Mater Sci.* 2005;33(4):501-509.
- Enakoutsa K, Leblond J-B. Numerical implementation and assessment of the GLPD micromorphic model of ductile rupture. *Eur J Mech A Solids.* 2009;28(3):445-460.
- Benallal A, Billardon R, Geymonat G. *Bifurcation and Localization in Rate-Independent Materials. Some General Considerations.* Springer; 1993.
- Mazars J, Pijaudier-Cabot G. From damage to fracture mechanics and conversely: a combined approach. *Int J Solids Struct.* 1996; 33(20–22):3327-3342.
- Geers MGD, de Borst R, Brekelmans WAM, Peerlings RHJ. Strain-based transient-gradient damage model for failure analyses. *Comput Methods Appl Mech Eng.* 1998;160(1–2):133-153.
- Lorentz E, Andrieux S. Analysis of non-local models through energetic formulations. *Int J Solids Struct.* 2003;40(12):2905-2936.
- Lorentz E, Besson J, Cano V. Numerical simulation of ductile fracture with the Rousselier constitutive law. *Comput Methods Appl Mech Eng.* 2008;197(21–24):1965-1982.
- Linse T, Huetter G, Kuna M. Simulation of crack propagation using a gradient-enriched ductile damage model based on dilatational strain. *Eng Fract Mech.* 2012;95(S1):13-28.
- Feld-Payet S, Besson J, Feyel F. Finite element analysis of damage in ductile structures using a nonlocal model combined with a three-field formulation. *Int J Damage Mech.* 2011;20(5):655-680.
- Reusch F, Svendsen B, Klingbeil D. Local and non-local Gurson-based ductile damage and failure modelling at large deformation. *Eur J Mech A Solids.* 2003;22(6):779-792.
- Al-Akhrass D, Bruchon J, Drapier S, Fayolle S. Integrating a logarithmic-strain based hyperelastic formulation into a three-field mixed finite element formulation to deal with incompressibility in finite-strain elastoplasticity. *Finite Elem Anal Des.* 2014;86(0):61-70.

17. Taylor RL. A mixed-enhanced formulation for tetrahedral finite elements. *Int J Numer Methods Eng.* 2000;47(1–3):205-227.
18. Miehe C, Apel N, Lambrecht M. Anisotropic additive plasticity in the logarithmic strain space: modular kinematic formulation and implementation based on incremental minimization principles for standard materials. *Comput Methods Appl Mech Eng.* 2002; 191(47–48):5383-5425.
19. Halphen B, Nguyen Q. Sur les matériaux standard généralisés. *J de Mécanique.* 1975;14:39-63.
20. Besson J, Steglich D, Brocks W. Modeling of crack growth in round bars and plane strain specimens. *Int J Solids Struct.* 2001; 38(46–47):8259-8284.
21. Lorentz E. *Lois de comportement à gradients de variables internes: construction, formulation variationnelle et mise en oeuvre numérique.* 1999, Université Pierre et Marie Curie-Paris VI.
22. Nguyen Q, Germain P, Suquet P. Continuum thermodynamics. *J Appl Sci.* 1983;50:1010-1020.
23. Mühlhaus H, Aifantis E. The influence of microstructure-induced gradients on the localization of deformation in viscoplastic materials. *Acta Mech.* 1991;89(1–4):217-231.
24. De Borst R, Mühlhaus HB. Gradient-dependent plasticity: formulation and algorithmic aspects. *Int J Numer Methods Eng.* 1992;35(3):521-539.
25. Sicsic P, Marigo J-J, Maurini C. Initiation of a periodic array of cracks in the thermal shock problem: a gradient damage modeling. *J Mech Phys Solids.* 2014;63:256-284.
26. Fortin M, Glowinski R. *Augmented Lagrangian methods: applications to the numerical solution of boundary-value problems.* 15 Elsevier; 2000.
27. Forest S. Micromorphic approach for gradient elasticity, viscoplasticity, and damage. *J Eng Mech.* 2009;
28. Zhang Y. *Modélisation et simulation numérique robuste de l'endommagement ductile.* 2016, PSL Research University.
29. Mialon P. *Eléments d'analyse et de résolution numérique des relations de l'élasto-plasticité.* Bulletin de la Direction des études et recherches-Electricité de France. Série C, mathématiques, informatique, 1986(3): p. 57–88.
30. Hai-Chang H. On some variational principles in the theory of elasticity and the theory of plasticity. *Acta Phys Sin.* 1954;10(3):259-290.
31. Washizu K. *On the variational principles of elasticity and plasticity.* 1955, [Cambridge]: M.I.T. Aeroelastic and Structures Research Laboratory.
32. Ern A, Guermond J-L. *Theory and Practice of Finite Elements.* 159 Springer Science & Business Media; 2013.
33. Auricchio F, Beirão da Veiga LC, Lovadina C, Reali A, Taylor R, Wriggers P. Approximation of incompressible large deformation elastic problems: some unresolved issues. *Comput Mech.* 2013;52(5):1153-1167.
34. Besson J, Steglich D, Brocks W. Modeling of plane strain ductile rupture. *Int J Plast.* 2003;19(10):1517-1541.
35. Lorentz E, Godard V. Gradient damage models: toward full-scale computations. *Comput Methods Appl Mech Eng.* 2011;200(21–22):1927-1944.
36. Miehe C, Welschinger F, Aldakheel F. Variational gradient plasticity at finite strains. Part II: local-global updates and mixed finite elements for additive plasticity in the logarithmic strain space. *Comput Methods Appl Mech Eng.* 2014;268(0):704-734.
37. Huetter G, Linse T, Muehlich U, Kuna M. Simulation of ductile crack initiation and propagation by means of a non-local Gurson-model. *Int J Solids Struct.* 2013;50(5):662-671.
38. Xue Z, Faleskog J, Hutchinson JW. Tension–torsion fracture experiments—part II: simulations with the extended Gurson model and a ductile fracture criterion based on plastic strain. *Int J Solids Struct.* 2013;50(25–26):4258-4269.
39. Cao TS, Maziere M, Danas K, Besson J. A model for ductile damage prediction at low stress triaxialities incorporating void shape change and void rotation. *Int J Solids Struct.* 2015;63:240-263.
40. Franklin A. Comparison between a quantitative microscope and chemical methods for assessment of non-metallic inclusions. *J Iron Steel Inst.* 1969;207(2):181-186.
41. Huespe AE, Needleman A, Oliver J, Sánchez PJ. A finite strain, finite band method for modeling ductile fracture. *Int J Plast.* 2012;28(1): 53-69.
42. Linse T, Kuna M, Viehrig HW. Quantification of brittle-ductile failure behavior of ferritic reactor pressure vessel steels using the Small-Punch-Test and micromechanical damage models. *Mater Sci Eng A.* 2014;614(0):136-147.
43. Koplik J, Needleman A. Void growth and coalescence in porous plastic solids. *Int J Solids Struct.* 1988;24(8):835-853.
44. Shinohara Y, Madi Y, Besson J. Anisotropic ductile failure of a high-strength line pipe steel. *Int J Fract.* 2016;197(2):127-145.

## APPENDIX A

### Elementary stiffness matrix for the 3-field element ( $\underline{u}, a, l$ )

To use the Newton-Raphson method to resolve the equations (95), a stiffness matrix should be computed. Expression of the second-order differential of  $\mathcal{L}$  is written as

$$\begin{cases} \delta^2 \mathcal{L}^u = \int_{\Omega_0} \delta \mathbf{E} : \frac{\partial \mathbf{T}}{\partial \mathbf{E}} : \delta \mathbf{E} + \delta \mathbf{E} : \frac{\partial \mathbf{T}}{\partial a} \delta a + \delta \mathbf{E} : \frac{\partial \mathbf{T}}{\partial l} \delta l + \mathbf{T} : \delta^2 \mathbf{E} d\Omega_0 \\ \delta^2 \mathcal{L}^a = \int_{\Omega_0} \delta a \left( -r \frac{\partial \kappa}{\partial \mathbf{E}} \right) : \delta \mathbf{E} + \delta a \left( r - r \frac{\partial \kappa}{\partial a} \right) \delta a + \delta a \left( 1 - r \frac{\partial \kappa}{\partial l} \right) \delta l + c (\delta \nabla a)^2 d\Omega_0 \\ \delta^2 \mathcal{L}^l = \int_{\Omega_0} \delta l \left( -\frac{\partial \kappa}{\partial \mathbf{E}} \right) : \delta \mathbf{E} + \delta l \left( 1 - \frac{\partial \kappa}{\partial a} \right) \delta a + \delta l \left( -\frac{\partial \kappa}{\partial l} \right) \delta l d\Omega_0 \end{cases} \quad (\text{A1})$$

or in a concise matrix form:

$$\delta^2 \mathcal{L} = \begin{bmatrix} \delta \mathbf{E} \\ \delta a \\ \delta l \end{bmatrix}^T \cdot \mathbf{\Pi} \cdot \begin{bmatrix} \delta \mathbf{E} \\ \delta a \\ \delta l \end{bmatrix} + c \delta \nabla a \cdot \delta \nabla a + \mathbf{T} : \delta^2 \mathbf{E}, \quad (\text{A2})$$

where the local stiffness matrix  $\mathbf{\Pi}$  issued from constitutive law is written:

$$\mathbf{\Pi} = \begin{bmatrix} \frac{\partial \mathbf{T}}{\partial \mathbf{E}} & \frac{\partial \mathbf{T}}{\partial a} & \frac{\partial \mathbf{T}}{\partial l} \\ \mathbf{SYM} & r - r \frac{\partial \kappa}{\partial a} & 1 - r \frac{\partial \kappa}{\partial l} \\ \mathbf{SYM} & \mathbf{SYM} & -\frac{\partial \kappa}{\partial l} \end{bmatrix}. \quad (\text{A3})$$

The variation of  $\mathbf{E}$  in A2 can be expressed in function of transformation tensor variation:

$$\begin{cases} \delta \mathbf{E} = \frac{\partial \mathbf{E}}{\partial \mathbf{C}} : \delta \mathbf{C} = \frac{\partial \mathbf{E}}{\partial \mathbf{C}} : (\mathbf{F}^T \cdot \delta \mathbf{F} + \delta \mathbf{F}^T \cdot \mathbf{F}) = \frac{2 \partial \mathbf{E}}{\partial \mathbf{C}} : (\mathbf{F}^T \cdot \delta \mathbf{F}) = \mathbb{P} : (\mathbf{F}^T \cdot \delta \mathbf{F}) \\ \mathbf{T} : \delta^2 \mathbf{E} = \delta \mathbf{C} : \mathbf{T} : \frac{\partial^2 \mathbf{E}}{\partial \mathbf{C} \partial \mathbf{C}} : \delta \mathbf{C} + \frac{\partial \mathbf{E}}{\partial \mathbf{C}} : \delta^2 \mathbf{C} \\ = (\delta \mathbf{F}^T \cdot \mathbf{F}) : \mathbf{T} : \mathbb{L} : (\mathbf{F}^T \cdot \delta \mathbf{F}) + \mathbf{T} : \mathbb{P} : (\delta \mathbf{F}^T \cdot \delta \mathbf{F}). \end{cases} \quad (\text{A4})$$

Here,  $\mathbb{P}$ ; is a fourth-order tensor defined as  $\mathbb{P} = \frac{2 \partial \mathbf{E}}{\partial \mathbf{C}}$ . One can find its expression in Miehe et al.<sup>18</sup>

In the discretized space, the unknown nodal variables are  $(\underline{U}, \underline{A}, \underline{L})$ . According to the definition in (96), one has the following expressions:

$$\begin{cases} \delta \mathbf{E} = \mathbb{P} : \mathbf{F}^T \cdot \delta \mathbf{F} = \mathbb{P} : (\mathbf{F}^T \cdot \mathbb{B}_g^u) \cdot \delta \underline{U} \\ \mathbf{T} : \delta^2 \mathbf{E} = (\delta \underline{U}^T \cdot \mathbb{B}_g^{uT} \cdot \mathbf{F}) : \mathbf{T} : \mathbb{L} : (\mathbf{F}^T \cdot \mathbb{B}_g^u \cdot \delta \underline{U}) + \mathbf{T} : \mathbb{P} : (\delta \underline{U}^T \cdot \mathbb{B}_g^{uT} \cdot \mathbb{B}_g^u \cdot \delta \underline{U}) \end{cases} \quad (\text{A5})$$

$$\begin{bmatrix} \delta \mathbf{E} \\ \delta a \\ \delta l \end{bmatrix} = \begin{bmatrix} \mathbb{P}_g : (\mathbf{F}^T \cdot \mathbb{B}_g^u) & 0 & 0 \\ 0 & \underline{N}^a & 0 \\ 0 & 0 & \underline{N}^l \end{bmatrix} \cdot \begin{bmatrix} \delta \underline{U} \\ \delta \underline{A} \\ \delta \underline{L} \end{bmatrix} = \mathbf{Q} \cdot \begin{bmatrix} \delta \underline{U} \\ \delta \underline{A} \\ \delta \underline{L} \end{bmatrix}. \quad (\text{A6})$$

With (A5) and (A6), the expression (A2) can be easily transformed in the discretized space:

$$\begin{aligned}
\delta^2 \mathcal{L} = & \sum_e \sum_g w_g \begin{bmatrix} \delta \underline{U} \\ \delta \underline{A} \\ \delta \underline{L} \end{bmatrix}^T \cdot \mathbf{Q}^T \cdot \mathbf{\Pi}_g \cdot \mathbf{Q} \cdot \begin{bmatrix} \delta \underline{U} \\ \delta \underline{A} \\ \delta \underline{L} \end{bmatrix} \\
& + c \delta \underline{A}^T \cdot \left( \mathbf{B}_g^a \right)^T \cdot \mathbf{B}_g^a \cdot \delta \underline{A} \\
& + \left( \mathbf{F}_g^T \cdot \mathbb{B}_g^\mu \cdot \delta \underline{U} \right)^T : \left( \mathbf{T}_g : \mathbb{L}_g \right) : \left( \mathbf{F}_g^T \cdot \mathbb{B}_g^\mu \cdot \delta \underline{U} \right) \\
& + \mathbf{T}_g : \mathbb{P}_g : \left( \delta \underline{U}^T \cdot \mathbb{B}_g^{\mu T} \cdot \mathbb{B}_g^\mu \cdot \delta \underline{U} \right).
\end{aligned} \tag{A7}$$

### Elementary stiffness matrix for the 5-field element ( $\underline{u}$ , $\theta$ , $P$ , $a$ , $l$ )

The stiffness matrix for the 5-field element can be derived from the second differential of equation (102):

$$\delta^2 \mathcal{L} = \int_{\Omega_0} \begin{bmatrix} \delta \mathbf{E} \\ \delta \theta \\ \delta P \\ \delta a \\ \delta l \end{bmatrix}^T \cdot \mathbf{Y} \cdot \begin{bmatrix} \delta \mathbf{E} \\ \delta \theta \\ \delta P \\ \delta a \\ \delta l \end{bmatrix} + (\mathbf{T}_D + P\mathbf{I}) : \delta^2 \mathbf{E} + c (\delta \nabla a)^2 d\Omega_0 \tag{A8}$$

with

$$\mathbf{Y} = \begin{bmatrix} \frac{\partial \tilde{\mathbf{T}}_D}{\partial \tilde{\mathbf{E}}} : \left( \mathbf{I} - \frac{1}{3} \mathbf{I} \otimes \mathbf{I} \right) & \frac{\partial \tilde{\mathbf{T}}_D}{\partial \tilde{\mathbf{E}}} : \frac{\mathbf{I}}{3} & \mathbf{I} & \frac{\partial \tilde{\mathbf{T}}_D}{\partial a} & \frac{\partial \tilde{\mathbf{T}}_D}{\partial l} \\ \text{SYM} & \frac{1}{9} \mathbf{I} : \frac{\partial \tilde{\mathbf{T}}}{\partial \tilde{\mathbf{E}}} : \mathbf{I} & -1 & \frac{1}{3} \mathbf{I} : \frac{\partial \tilde{\mathbf{T}}}{\partial a} & \frac{1}{3} \mathbf{I} : \frac{\partial \tilde{\mathbf{T}}}{\partial l} \\ \text{SYM} & \text{SYM} & 0 & 0 & 0 \\ \text{SYM} & \text{SYM} & \text{SYM} & r - r \frac{\partial \kappa}{\partial a} & 1 - r \frac{\partial \kappa}{\partial l} \\ \text{SYM} & \text{SYM} & \text{SYM} & \text{SYM} & \frac{\partial \kappa}{\partial l} \end{bmatrix}. \tag{A9}$$

Similar to (A6) and (A7), in the discretized space, (A8) can be written as follows:

$$\begin{aligned}
\delta^2 \mathcal{L} = & \sum_e \sum_g w_g \begin{bmatrix} \delta \underline{U} \\ \delta \underline{\theta} \\ \delta \underline{P} \\ \delta \underline{A} \\ \delta \underline{L} \end{bmatrix}^T \cdot \mathbf{S}^T \cdot \mathbf{Y}_g \cdot \mathbf{S} \cdot \begin{bmatrix} \delta \underline{U} \\ \delta \underline{\theta} \\ \delta \underline{P} \\ \delta \underline{A} \\ \delta \underline{L} \end{bmatrix} + c \delta \underline{A}^T \cdot \left( \mathbf{B}_g^a \right)^T \cdot \mathbf{B}_g^a \cdot \delta \underline{A} \\
& + \left( \mathbf{F}_g^T \cdot \mathbb{B}_g^\mu \cdot \delta \underline{U} \right)^T : \left( (\mathbf{T}_D + P\mathbf{I})_g : \mathbb{L}_g \right) : \left( \mathbf{F}_g^T \cdot \mathbb{B}_g^\mu \cdot \delta \underline{U} \right) \\
& + (\mathbf{T}_D + P\mathbf{I})_g : \mathbb{P}_g : \left( \delta \underline{U}^T \cdot \mathbb{B}_g^{\mu T} \cdot \mathbb{B}_g^\mu \cdot \delta \underline{U} \right),
\end{aligned} \tag{A10}$$

where

$$\mathbf{S} = \begin{bmatrix} \mathbb{P}_g: (\mathbf{F}^T, \mathbb{B}_g^u) & 0 & 0 & 0 & 0 \\ 0 & \underline{N}^\theta & 0 & 0 & 0 \\ 0 & 0 & \underline{N}^p & 0 & 0 \\ 0 & 0 & 0 & \underline{N}^a & 0 \\ 0 & 0 & 0 & 0 & \underline{N}^l \end{bmatrix} \quad (\text{A11})$$

### Stiffness matrix for the constitutive equations at Gauss points

In the expressions (A3) and (A9), the differential of  $\mathbf{T}$  and  $\kappa$  with respect to  $(\mathbf{E}, a, l)$  at the Gauss point level must be computed.

Gather here the equations (61) and (66):

$$\begin{cases} \mathbf{T} = \mathbf{T}^e - \mathbb{E}:\Delta\mathbf{E}^p \\ \Delta\mathbf{E}^p = \frac{\Delta\kappa\partial T^*}{J\partial\mathbf{T}} \end{cases} \quad (\text{A12})$$

Note  $\mathbf{v} = \frac{\partial T^*}{\partial\mathbf{T}}$  whose expression is given by (68), and the differential of  $\mathbf{T}$  is

$$\dot{\mathbf{T}} = \mathbb{E}:\dot{\mathbf{E}} - \frac{1}{J}(\Delta\kappa\mathbb{E}:\mathbf{v} + \Delta\kappa\mathbb{E}:\dot{\mathbf{v}}). \quad (\text{A13})$$

Then according to (67), one gets

$$\Delta\kappa = \frac{\left(\frac{\dot{T}^*}{J} + \dot{l} + r\dot{a}\right)}{r + A'} = \frac{1}{r + A'}\left(\frac{\mathbf{v}:\dot{\mathbf{T}}}{J} + \dot{l} + r\dot{a}\right), \quad (\text{A14})$$

where  $A' = \frac{dA}{d\kappa}$ .

By definition of  $\mathbf{v}$ , one has

$$\dot{\mathbf{v}} = \left(\frac{\partial\mathbf{v}}{\partial\mathbf{T}} + \frac{\partial\mathbf{v}}{\partial T^*} \otimes \mathbf{v}\right):\dot{\mathbf{T}}. \quad (\text{A15})$$

Now after combining (A13-A15) and one obtains

$$\mathbb{M}:\dot{\mathbf{T}} = \mathbb{E}:\dot{\mathbf{E}} - \frac{\mathbb{E}:\mathbf{v}}{r + A'}(\dot{l} + r\dot{a}), \quad (\text{A16})$$

where  $\mathbb{M} = \left[\mathbb{I} + \frac{1}{J^2(r + A')} \mathbb{E}:\mathbf{v} \otimes \mathbf{v} + \frac{\Delta\kappa}{J} \mathbb{E}:\left(\frac{\partial\mathbf{v}}{\partial T^*} \otimes \mathbf{v} + \frac{\partial\mathbf{v}}{\partial\mathbf{T}}\right)\right]$  is a fourth-order tensor.

As a result,

$$\dot{\mathbf{T}} = \mathbb{M}^{-1}:\left[\mathbb{E}:\dot{\mathbf{E}} - \frac{\mathbb{E}:\mathbf{v}}{J(r + A')}(\dot{l} + r\dot{a})\right]. \quad (\text{A17})$$

The differential of  $\kappa$  with respect to  $(\mathbf{E}, a, l)$  can be obtained by substituting (A17) in (A14).



### Stiffness matrix for the constitutive equations at Gauss points for singular case

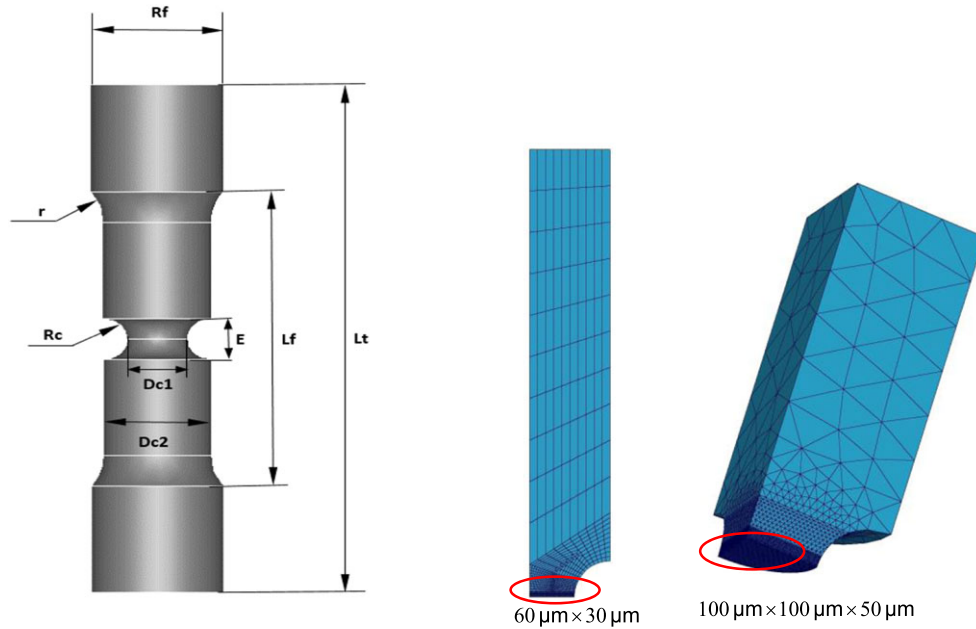
In this part, the stiffness matrix for the special case ( $T^* = 0$ ) that was presented in Section 3.2 will be given. According to (84) and (85), one derives

$$\begin{cases} \dot{\mathbf{T}} = 0 \\ \dot{\kappa} = \frac{1}{A' + r}(l + r\dot{a}) \end{cases} \quad (\text{A18})$$

From (A18), it is noted that if the case  $T^* = 0$  occurs, the kinematic part in the stiffness matrix is zero:  $\frac{\partial \mathbf{T}}{\partial \mathbf{E}} = 0$ . Thus, to ensure the stiffness matrix could be inverted, some arbitrary additional stiffness is added by letting  $\frac{\partial \mathbf{T}}{\partial \mathbf{E}} = \xi \mathbb{E}$ , with  $\xi \leq 10^{-5}$ .

### Specimen geometries and used FE meshes

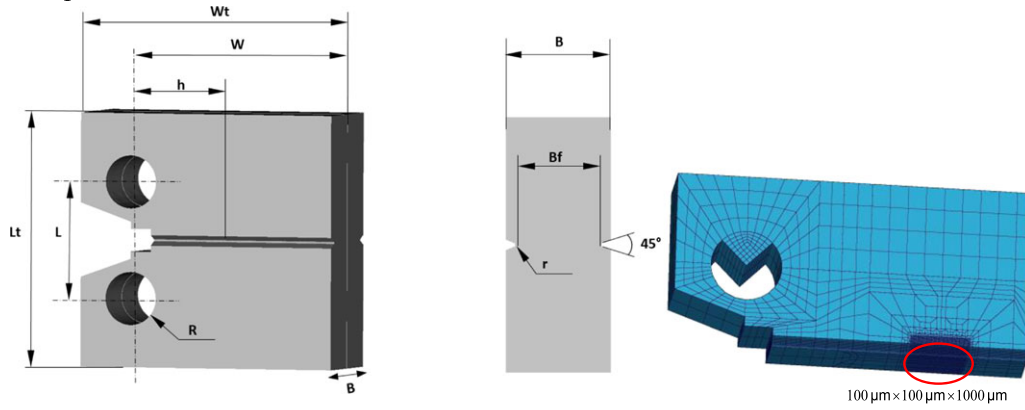
NT specimens



Specimens	Rc (mm)	E (mm)	Dc1 (mm)	Dc2 (mm)	Df (mm)	Lt (mm)	Lf (mm)	Rf (mm)
NT2	2	4	10	18	22	100	58	10
NT4	4	8	10	18	22	100	58	10
NT10	10	16	10	18	22	100	58	10

**FIGURE A1** Geometries and meshes of notched tensile (NT) specimens

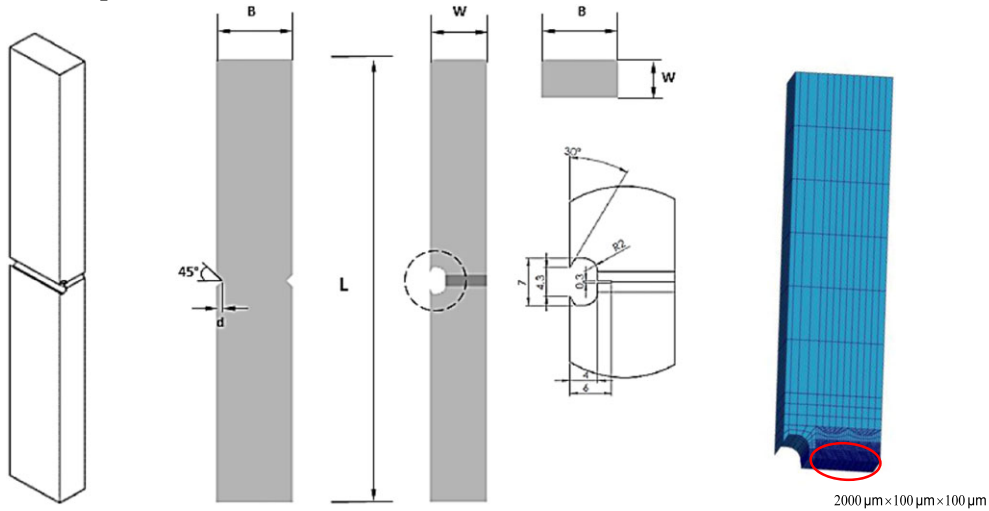
CT specimens



	B (mm)	Bf (mm)	W (mm)	L (mm)	R (mm)	h (mm)	Wt (mm)	Lt (mm)	r (mm)
CT20	20	18.4	16	22	5	20	50	48	0.25
CT12.5	12.5	18.4	16	22	5	20	50	48	0.25

FIGURE A2 Geometries and meshes of compact tension (CT) specimens

SENT specimens



	L (mm)	B (mm)	W (mm)	d (mm)	R2 (mm)
SENT20	230	20	15	1.5	2

FIGURE A3 Geometries and meshes of single edge notched tensile (SENT) specimen